Master's thesis

NTNU
Norwegian University of Science and Technology
Faculty of Natural Sciences
Department of Materials Science and Engineering

Herman Hanssen

Development of aluminium alloys with superior properties for additive manufacturing

Master's thesis in Materials Science and Engineering
Supervisor: Yanjun Li
Co-supervisor: Yijiang Xu, Eivind Johannes Øvrelid, Freddy Leijon and Kai Zhang

June 2022

NTNU
Norwegian University of Science and Technology

Herman Hanssen

Development of aluminium alloys with superior properties for additive manufacturing

Master's thesis in Materials Science and Engineering
Supervisor: Yanjun Li
Co-supervisor: Yijiang Xu, Eivind Johannes Øvrelid, Freddy Leijon and Kai Zhang
June 2022

Norwegian University of Science and Technology
Faculty of Natural Sciences
Department of Materials Science and Engineering

NTNU
Norwegian University of
Science and Technology

Preface

The work of this master thesis has been performed at Department for Material Science and Engineering at NTNU in the spring of 2022.

I want to thank Yingda Yu, Ingvild Runningen and Stefanie Lode for their help at different labs during this work.

A special thanks goes out to my supervisor Yanjun Li and co-supervisors Yijiang Xu, Eivind Johannes Øvrelid, Freddy Leijon and Kai Zhang for their help and guidance.

Trondheim, June 2022

Herman Hanssen

Abstract

Additive manufacturing (AM) techniques such as selective laser melting (SLM) and other powder bed fusion (PBF) methods is widely used to produce components with high geometric complexity and excellent physical properties. Ultra-high cooling rates make it possible to create a fine-grained structure and supersaturate the matrix with alloying elements. However, compared to traditional techniques, few alloys are readily available for AM, and many alloys used in AM are based on modified cast alloys. New alloys need to be developed for AM to reach its true potential. In this master project a research focus has been put on the development of Al-Si based alloys with superior properties. In the first part, with the aim to determine optimal chemical compositions, a thin film of Al-Si-Cr with a concentration gradient was deposited onto an aluminium substrate by using physical vapour deposition (PVD). Laser surface remelting of the film was performed to mimic the SLM conditions. Characterization of the remelted zones revealed pores and cracks in certain alloys, however desirable microstructures were also found. Hardness mapping showed an increased hardness with increasing content of silicon and chromium. Two alloys, Al-Si12.6-Cr10.6 and Al-Si9.9-Cr10.6, showed a promising microstructure with small and evenly distributed particles in the remelted zone.

In the second part, two aluminium-silicon-copper alloys were designed and cast in a wedge-shaped copper mould. The high cooling rate in the tip of the wedge casting and the subsequent laser surface remelting were used to mimic the SLM process, from powder production to fabrication of components. A significant grain refinement was achieved in the laser remelted zone of both alloys. As a result the remelted zone show a much higher hardness than the bulk material.

Sammendrag

Selektiv laser smelting og andre pulverbaserte 3D-printing-metoder kan produsere komponenter med høy geometrisk kompleksitet og med suverene fysiske egenskaper. Den høye avkjølingshastigheten fører til en finkornet struktur og gjør det mulig å få en matriks overmettet på legeringselementer. Sammenlignet med tradisjonelle metoder er det få kommersielt tilgjengelige legeringer egnet for additiv tilvirking og mange av de brukte legeringen er gamle støpelegeringer modifisert for additiv tilvirkning. For at additiv tilvirking skal nå sitt fulle potensial må nye legeringer utvikles. En plate med en gradientfilm bestående av aluminium, silisium og krom, produsert med fysisk dampavsetning, ble overflatesmeltet med en laser. Lasersmeltingen imiterer forholdene til selektiv laser smelting og gir en lignende mikrostruktur. Hardhetsmålinger av overflaten viste en trend med økende hardhet med økende innhold av silisium og krom. En kartlegging av sprekkdannelse på overflaten visste sprekkdannelse i et lite legeringsintervall. To legeringer, Al-Si12.6-Cr10.6 and Al-Si9.9-Cr10.6, viste en lovende mikrostruktur med fine partikler jevnt fordelt i strukturen.

To aluminium-silisium-kobber-legeringer ble utviklet og støpt i en kileformet kobber-støpeform. Den høye avkjølingshastighet i tuppen av den kileformede støpeformen etterligner forholdene i pulverproduksjon, mens den etterfølgende lasersmelting imiterer forholdene til selektiv laser smelting. De omsmeltede sonene til begge legeringer hadde betydelige mindre korn enn bulkmaterialet og likeaksede kornstruktur ble oppnådd.

Table of Contents

List of Figures

List of Tables

1 Introduction

Selective laser melting (SLM) is an additive manufacturing (AM) technique capable of producing metallic parts with high geometric complexity, without the need for special tools or multiple processing steps. This is possible because components are produced layer by layer, which provides high design freedom [1]. Selective laser melting can produce structures made of aluminium alloys, steel alloys, titanium alloys, nickel-based alloys and other metallic materials [2].

The desirable properties of aluminium have made it an essential material in many applications. Aluminium is widely used in the automotive, maritime and aerospace industries. High specific strength, low weight and good corrosion resistance make aluminium alloys applicable in numerous situations. Additive manufacturing of aluminium alloys is therefore of great interest. The cooling rate of the SLM process, which is significantly higher than the cooling rates found in traditional casting techniques, can be utilized to refine the grain structure and to trap elements in solid solution. However, many high performing aluminium alloys, for example, the 6000 and 7000 series, are not suited for the high cooling rates and steep temperature gradients that are found in many additive manufacturing techniques [3]. Ill-suited alloys will, under these conditions, produce coarse columnar grains, resulting in poor mechanical properties and a high risk of crack formation.

Several alloy development methodologies for additive manufacturing have been reported in the literature. Q. Jia et al. [4] developed an Al-Mn-Sc alloy by casting it in a wedge shaped mould followed by laser surface remelting of the wedge tip. They confirmed the alloys' suitability for AM by producing parts with SLM, the as-built part had a yield strength of 430 MPa, which increased to 570 MPa after heat treatment. M. Moorehead et al. [5] created a method with high throughput by using direct energy deposition. By mixing single element powders they were able to directly print several alloy combinations for characterization. J.H. Martin [6] et al. introduced nanoparticles into the powder feedstock of high performing aluminium alloys, which by them self are unsuited for AM. The nanoparticles resolved the issues of columnar dendritic structure previously encountered when printing these alloys, and the alloys displayed a refined and equiaxed microstructure without cracks.

Two methodologies of alloy development for additive manufacturing will be tested in this work. The first method is based on the physical vapour deposition of a composition gradient film on a substrate plate. A film of aluminium, silicon and chromium will be deposited on an aluminium substrate. The relative positions of the respective target metals during deposition create a film with variation in chemical composition along the two surface axis. The deposited surface will be subjected to laser surface remelting to imitate the conditions of SLM. The second method includes designing and casting of two Al-Si-Cu alloys in a wedge shaped copper mould. In the tip of the wedge mould the cooling rate of the melt is similar to the cooling rates associated with the gas atomization process, which is commonly used to produce powders for SLM [7] [8]. The tip of

the wedge cast will be scanned with a laser in a SLM machine to cause melting of the surface. The wedge casting combined with the laser surface remelting will subject the alloys to conditions comparable to those found in the SLM process. The remelted structures will be characterized to determine if these alloys are suitable for SLM.

The objective of this work is to investigate the aluminium-silicon-chromium alloy system and recommend one or more alloys from this system which could be suitable for AM. This project also aims to determine if the two developed aluminium-copper alloys are suitable for AM.

2 Theory

This part is inspired by the theory section in my specialization project, "Development of super aluminium alloys for additive manufacturing".

2.1 Aluminium alloys

Aluminium alloys are the most used group of construction materials after steel and iron. High strength to weight ratio, good corrosion resistance, and outstanding thermal and electric conductivity make them desirable in numerous applications [9]. Aluminium alloys can be divided into cast aluminium alloys and wrought aluminium alloys, and these can further be classified as heat-treatable, and non-heat-treatable alloys [10]. Table 1 shows a common classification of wrought aluminium alloys based on their main alloying element.

Series	Elements	Heat-treatability
1xxx	Pure Al	Non-heat-treatable
2xxx	Al-Cu	Heat-treatable
3xxx	Al-Mn	Non-heat-treatable
4xxx	Al-Si	Non-heat-treatable
5xxx	Al-Mg	Non-heat-treatable
6xxx	Al-Mg-Si	Heat-treatable
7xxx	Al-Zn	Heat-treatable

Table 1: Classification of wrought aluminium alloys based on the main alloying element.

2.1.1 Strengthening

Aluminium in its pure form is a weak metal, with a tensile strength of 70-100 MPa. However, several methods of strengthening exist. The strengthening mechanisms in aluminium alloys are

grain boundary strengthening, solid-solution strengthening, strain hardening, and precipitation hardening[10] [11].

Grain boundary strengthening is one of the most important strengthening mechanisms in aluminium alloys and other metals. Plastic deformation will cause deformations to travel through the matrix. Grain boundaries will hinder the movement of dislocations due to the difference in crystallographic orientation between two neighbouring grains. A material with small grains will have a larger total grain boundary area and therefore be more effective in stopping moving dislocations [11] [10]. Reducing the grain size also has the advantage of increasing the toughness of the material. The Hall-Petch equation describes the relationship between yield strength (σ_y) and average grain diameter(d):

$$\sigma_y = \sigma_0 + k_y d^{-\frac{1}{2}} \tag{1}$$

where k_y and σ_0 are material constants.

Solid-solution strengthening is the process of strengthening metal by introducing impurity atoms into the matrix. The presence of impurity atoms in an atomic matrix will cause lattice strains, which will impede the movement of dislocations [11]. An increased presence of dislocations will also increase the strength of the material. This is because the strain field around a dislocation will hinder the movement of other dislocations. This phenomenon is called work hardening. The dislocation density will increase as the material is plastically deformed, meaning that the material will become stronger during deformation.

Precipitation hardening is achieved through a series of heat treatment steps. The material is first heat-treated at a higher temperature (~ 600°C) for some time, at this temperature, the solubility of alloying elements is high. The following quenching makes the material supersaturated with alloying elements. The material is then heat-treated at a lower temperature (~ 200°C), which facilitates the formation of small particles called precipitates. After a suitable ageing time, the material is quenched. The precipitates are evenly distributed in the matrix and increase the strength of the alloy.

2.1.2 Alloying elements used in this work

Silicon as an alloying element provides aluminium alloys with several desirable properties. Silicon lowers the viscosity of the aluminium melt, which makes it flow easier. Silicon also reduces volume shrinkage during solidification, which is due to the fact that silicon expands during solidification. Silicon will therefore compensate for the solidification shrinkage of aluminium. Casting alloys often have a silicon content close to the eutectic composition. Alloys close to the eutectic composition have short solidification ranges, which reduces the risk of solidification cracking. Silicon also

increases the strength of the alloy through solid-solution-strengthening [10].

Chromium is often added to Al-Mg-Si and Al-Mg-Zn alloys, and the amount of Cr is generally not above 0.35 wt%. Chromium is added to control the grain structure, reduce grain growth and prevent recrystallisation at higher temperatures. Chromium also makes aluminium alloys less susceptible to stress corrosion cracking and increases the toughness of aluminium alloys [12].

Titanium is added as a grain refiner to aluminium alloys to reduce the average grain size. During solidification Al_3Ti is a very good nucleation site for α-aluminium; more nucleation sites mean that more grains will nucleate, resulting in a finer grain structure. Titanium also has a high growth restriction factor, making it effective in expanding the zone of constitutional undercooling, which is needed for nucleation to occur [13] [14].

Copper increases the strength of the aluminium alloys through solid solution hardening. Adding copper also makes it possible to increase the strength via precipitation hardening. Manganese also increases strength due to solid solution hardening. Also, combined with silicon manganese makes precipitation hardening possible. Zirconium also makes the alloy stronger, and the formation Al_3Zr-particles can inhibit recrystallisation [15] [16]. Al_3Zr-particles can also work as an effective heterogeneous nucleation site for α-aluminium, due to the low amount of interatomic spacing mismatch, and therefore provide refinement of the grain structure [17].

2.2 Selective laser melting

Selective laser melting (SLM) and electron beam melting (EBM) both fall under the category of powder bed fusion (PBF) additive manufacturing techniques. PBF methods all utilize a laser or electron beam to fuse the powder together, either by melting or sintering. A schematic setup of the SLM process is shown in figure 2.1. The powder is distributed to the build platform by the recoater and then scanned with the laser. Once the scan of one layer is completed the build platform is lowered, the powder reservoir is lifted, and more powder is distributed by the recoater. The recoater normally works similar to what is shown in figure 2.1, but some new SLM machines have recoaters that apply powder from above. The process of lowering the build platform, applying new powder and laser scanning is repeated until the build is completed. SLM and SLS are performed in an enclosed chamber filled with an inert gas, usually argon, while EBM is performed in a vacuum [18] [19].

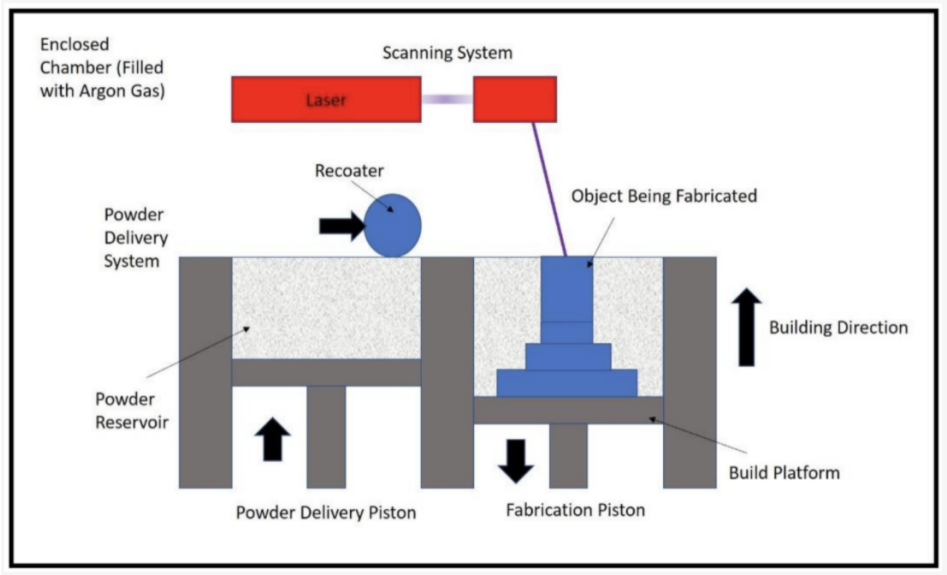

Figure 2.1: Typical setup of the SLM process [20].

Compared to other popular AM techniques, SLM has a low deposition rate. The deposition rate of aluminium in SLM is in the vicinity of 10 g/min, while wire and arc additive manufacturing (WAAM) can deposit several hundred grams of aluminium per minute [21] [22], this makes WAAM more suited than SLM for producing large components. However, WAAM has less geometrical precision than SLM. SLM also provides superior mechanical properties compared to WAAM, this is because of the higher cooling rate associated with SLM. The cooling rates of SLM are usually in the range of 10^4 to 10^6 K/s [4]. Such high cooling rates make it possible to achieve a high degree of grain refinement. The high cooling rate also makes it possible to trap a lot of alloying elements in solid solution, making the alloy stronger. If the alloys then are subjected to an appropriate heat treatment, the strength can be increased even further.

One major concern regarding SLM and other AM techniques is the quality of the components produced. Due to the large number of parameters involved in the SLM process, the properties of the finished part can be difficult to control. Porosity, hot cracking, poor surface finish and anisotropy are all problems that can occur from the SLM process [23]. Scan speed, laser power, hatch spacing and layer thickness are process parameters associated with the SLM process. If the wrong combination of parameters is chosen, defects are bound to occur. Common defects are porosity, cracks and balling, all of which will compromise the quality of the component [7]. The specific laser energy, Ψ (J/mm^3), is commonly used during the optimization of SLM parameters.

$$\Psi = \frac{P}{v \cdot h \cdot d} \tag{2}$$

Where P is the laser power (W), v is the scan speed (mm/s), h is the hatch spacing (mm), and d is the layer thickness (mm). This means the energy density will increase with increasing laser power

and with decreasing scan speed, hatch distance and layer thickness. For single-line laser scans, the line energy (energy per unit length) can be calculated by [24]

$$Q = \frac{P}{v} \tag{3}$$

Where Q is the line energy. High laser power is required to cause melting of aluminium powders. This is due to the high reflectivity and thermal conductivity of aluminium alloys. Common engineering metals such as stainless steel 316 and Ti64 have a reflectivity of 60% and 53-59 %, respectively, while AlSi10Mg have a reflectivity of 91% [19]. This means that a lot of the laser energy is not absorbed by the powder, the heat generated by the laser is also effectively transported away due to the high thermal conductivity. Therefore, a high laser power is required to cause aluminium powders to melt.

Mitigating porosity is a key aspect when producing aluminium parts with selective laser melting. Pores reduce the stress-bearing area and cause concentration of stress. Hydrogen pores are the most common form of porosity. The small and spherical hydrogen pores (also called metallurgical pores) arise due to trapped hydrogen (or other gases) [7]. This happens because the high solidification rates of SLM do not give the gas bubbles enough time to escape. An important reason for the formation of hydrogen pores is the large difference in the solubility of hydrogen in liquid and solid aluminium. Since the solubility of hydrogen is very low in solid aluminium the last liquid to solidify will be enriched with hydrogen. If the melt is supersaturated with hydrogen, gas bubbles will easily form [25]. Another form of porosity that can occur in SLM produced components is keyhole pores, keyhole pores are bigger and more irregularly shaped than hydrogen pores [19]. Keyhole pores are created due to instabilities in the keyhole, i.e. the metal solidifies before filling the keyhole. Generally, hydrogen porosity occurs at low scanning speeds and keyhole porosity at high scanning speeds [19].

Finding the optimal combination of parameters is an effective approach to reduce the porosity of components produced with SLM. Kimura et al. were able to achieve a relative density of 99.8 % by optimizing the process parameters [26]. It was shown that the relative density of the as-built part decreased at both higher and lower laser energy than the optimal value. Porosity formation at low laser energy was caused by incomplete melting of powder. While the porosity forming at higher laser energy was characterized as metallurgical pores. Which was thought to arise from released hydrogen or trapped argon from the chamber. One measure to reduce hydrogen-induced porosity is to reduce the humidity of the powder. Drying the powder in a furnace has shown great results in reducing hydrogen porosity in parts fabricated with SLM. Weingarten et. al [27] showed that porosity may be reduced by 35 % with a drying temperature of 90 °C and 50 % with a drying temperature of 200 °C. They also investigated the possibility of drying the powder inside the production chamber. This was done by scanning each layer twice. The first time the whole surface was scanned with a low laser power, which had a drying effect on the powder without

melting it (pre-sinter). The second scan was done with a higher power to cause fusion according to the design. This approach was able to reduce the density of hydrogen pores by up to 90 %, depending on the scan speed and laser beam diameter. This pre-sinter scan strategy has also been proven effective by N. T. Aboulkhair, et al. [19]. Among other things, they investigated which scan strategy that was most effective in reducing porosity. Among the six scan strategies investigated, the pre-sinter scan strategy produced the highest density parts, reaching a density of 99.82%. The pre-sinter scan strategy they used scanned each layer twice, where the first scan is done with half power. R.Rashid et al. [28] found that a scan strategy which scanned each layer twice resulted in higher hardness of as-built stainless steel components. Figure 2.2 shows some common scan strategies used in SLM.

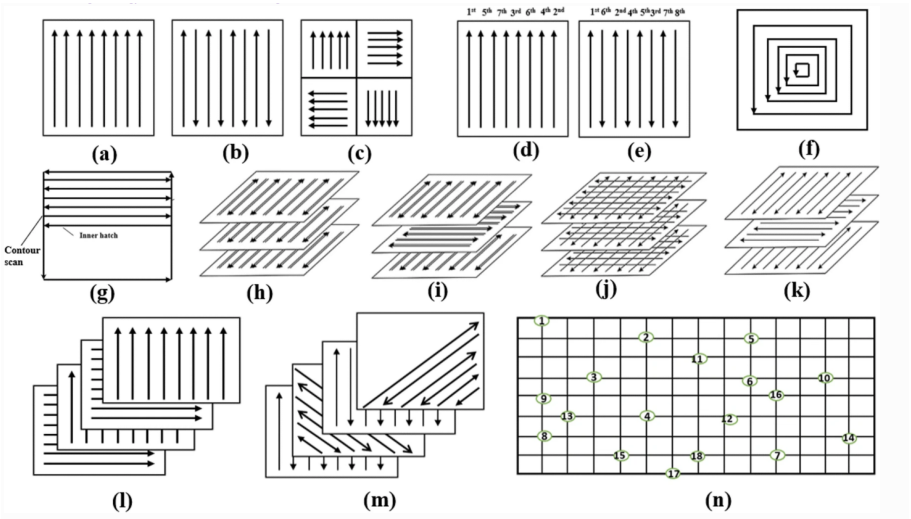

Figure 2.2: Different laser scan strategies that can be used in SLM [29].

The hatch spacing is the distance between two scanned lines. Together with the melt pool width, the hatch spacing provides information about the amount of overlap between scanned lines. If the hatch spacing is too large it can lead to incomplete melting of powder. If the following criterion holds, the overlap between tracks is large enough to cause complete melting [30].

$$\left(\frac{h}{W}\right)^2 + \left(\frac{d}{D}\right)^2 \leq 1 \tag{4}$$

where h is the hatch spacing, W is the melt pool width, d is the layer thickness, and D is the melt pool depth. Ming Tang et al. [30] investigated the effect different hatch spacings had on fatigue life, elongation and yield strength [30]. Three different hatch spacings were used (0.16mm, 0.19mm and 0.22mm). Smaller hatch spacing was associated with better fatigue and elongation properties. While the highest yield strength was achieved with a hatch spacing of 0.19mm.

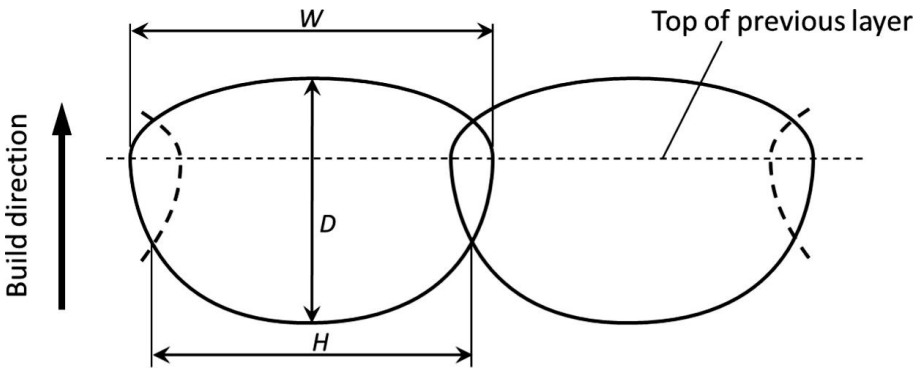

Figure 2.3: Cross-section geometry of a scanned track [30].

It is important to consider the amount of oxygen in the protective atmosphere when trying to reduce porosity. Due to aluminium's high affinity to oxygen oxidation can easily occur during the SLM process [19]. Oxidation promotes porosity, therefore SLM is performed in an inert environment. It has been found that defects in aluminium alloys have a high oxygen content, suggesting that oxidation is the cause of these defects [7]. If oxidation occurs it prevents good bonding between scanned lines and tracks, which could lead to porosity and cracks [31].

Another common defect than can occur during the SLM process is balling. Balling is the formation of spherical particles on the surface. If the surface tension is too great, it will prevent the molten metal to distribute evenly [32]. The balling effect negatively impacts the quality of the part in several ways.

1. Balling increases the surface roughness of the part, possibly introducing the need for post production surface treatments [33].
2. Porosity can easily form in the spaces between the spherical particles [33].
3. If the balling effect becomes extreme, it could hinder or damage the recoater [33].

Reducing the oxygen content of the production atmosphere to a sufficiently low level, can mitigate the balling effect to a large degree. One of the reasons for this is that the oxide film on the surface worsens the wetting between liquid and solid aluminium [31] [33]. The process parameters also play an important role when trying to minimize balling. Balling can occur both at low and high energy inputs, meaning that an ideal energy input value exist. Also, a too high scan speed can cause spatter which could lead to balling [32] [33].

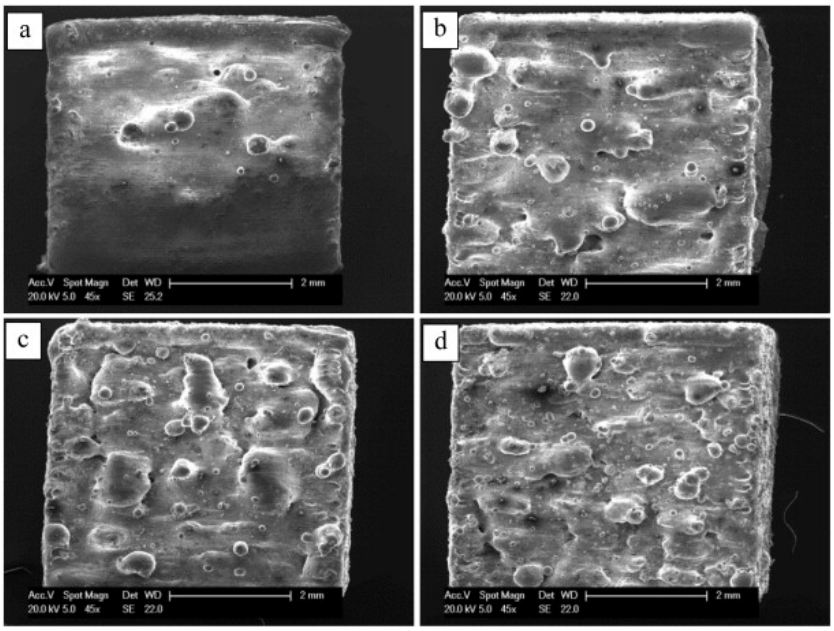

Figure 2.4: Balling effect on AlSi10Mg component produced with selective laser melting [19].

Hot cracking, or solidification cracking, is yet another defect than can be encountered in SLM. Solidification cracking occurs in the temperature zone between the liquidus and solidus, where solid and liquid both are present. If the alloy experiences a large amount of tensile stress during solidification hot cracking can occur. During growth of columnar dendrites the space between dendrites can get enclosed. If the rate of feeding is smaller than the rate of shrinkage in these regions, hot cracking can take place. In order to avoid hot cracking, the shrinkage that the alloy experiences due to solidification needs to be accounted for by a supply of liquid metal. An alloy with a wide solidification range is more likely to experience hot cracking, because the strain values are larger [34] [35] [36]. A simple and effective way of reducing the susceptibility to hot cracking is therefore to use an alloy close to the eutectic composition.

2.2.1 Mechanical properties of aluminium produced with SLM

The mechanical properties of aluminium alloys produced with SLM can be significantly different compared to those of cast aluminium. The big difference in cooling rate, means that the fineness of the microstructure will be different. The SLM process has a very high cooling rate and usually produces components with a very fine microstructure, traditional casting have a slower cooling rate and therefore often a coarser microstructure [37]. The mechanical properties of SLM produced aluminium alloys can exceed that of their cast counterparts. N. T. Aboulkhair et al. [37] produced components of AlSi10Mg with yield strength that exceeded the yield strength of a A360 die cast alloy, which is the cast alloy most comparable to AlSi10Mg. However, the die cast A360 had better ductility than the SLM AlSi10Mg. N. Read et al. [38] achieved similar result with SLM produced AlSi10Mg, that had superior yield strength, but inferior elongation compared to A360 die cast

alloy.

Components produced with SLM may have anisotropic mechanical properties. This is due to the formation of columnar grains. Columnar grains is formed parallel to the build direction and perpendicular to the scan direction [23]. It has however, been shown that an isotropic microstructure is achievable by applying an appropriate laser scan strategy [28].

2.2.2 Surface quality

Although the surface quality of SLM and other PBF techniques are better than those of other AM techniques, poor surface quality can still occur [39]. There are several phenomena that can worsen the surface finish of SLM produced components. These include the stair-case effect which arises due to the layer-by-layer production, spattering, balling effects and melt pool instabilities. Depending on the design, support structures may be needed during production. The removal of these support structures could aggravate the surface quality of the part [40]. The surface quality is of special concern for parts intended for cyclic loading. Surface irregularities will act as stress raisers, which lower the fatigue life. In the work performed by Uhlmann et al. it was found that the high cyclic fatigue life was clearly increased after surface treatment of SLM parts [41].

Multiple surface treatments cam improve the surface quality of components. Such as machining, shot peening, rolling and laser polishing. Figure 2.5 shows improved surface quality after laser polishing.

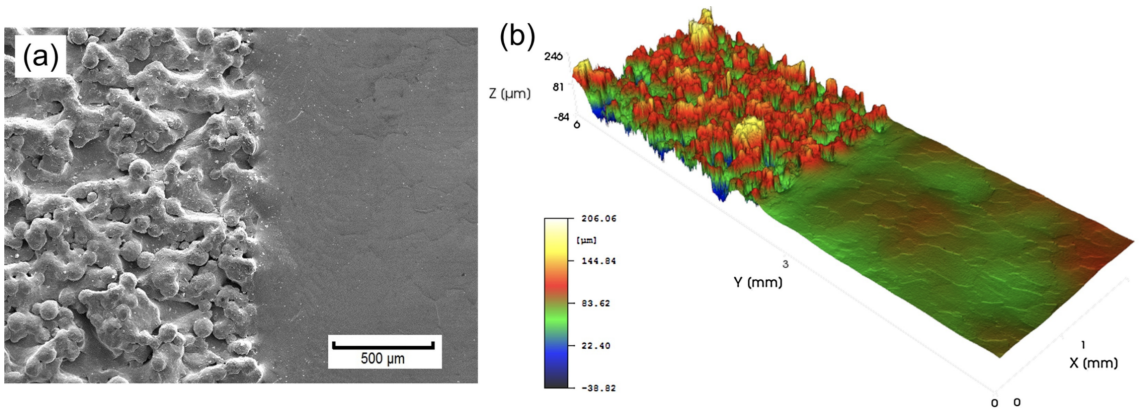

Figure 2.5: Improved surface quality after laser polishing, a) SEM picture, b) 3D micrograph. Source: [40]

2.3 Solidification theory

Solidification is the combined result of nucleation and undercooling. The early stages of solidification is predominately controlled by nucleation. Nucleation needs a certain amount of undercooling to take place and nucleation rate will increase with increasing undercooling. The formation of new

grains will release latent heat, which may cause the temperature of the system to rise. Beyond this point where the temperature rises due to the formation of new grains, nucleation is minimal and solidification will be mainly controlled by growth of previously nucleated grains. Nucleation in metal melts will mainly occur on already existing solids, i.e. heterogeneous solidification. The opportunity for nucleating crystals to grow on a solid surface, reduces the amount of undercooling that is needed for nucleation to take place [34] [42].

The overall undercooling needed is composed of kinetic undercooling, thermal undercooling, constitutional undercooling and curvature undercooling. The kinetics of atom transfer can for some crystals play a significant role during growth. For metals and other non-faceted substances atomic transfer from liquid to solid is so fast that the kinetic undercooling can be neglected. However, for substances with a faceted growth morphology the kinetics may have a great impact on growth. The surface of a faceted material is flat on the atomic scale, this means that there are few favourable sites for new atoms to attach. A favourable site is a site with several neighbouring atoms to attach to, the first atom to attach to a flat surface will only have one neighbouring atom and could easily detach. On the other hand, a non-faceted interface is atomically rough, meaning that many suitable positions are exposed. When few sites are available for atoms to attach to, the rate of detachment will be high and more undercooling is needed for growth to continue. Pure metals can undercool far beneath the liquidus temperature, if no nucleation takes place. The melt is then said to be thermally undercooled [34] [42]. If the partition coefficient of an alloys is less than one, the liquidus temperature of that alloy will increase with increase purity concentration, which can be seen from the phase diagram in figure 2.6. Due to the solute rejection during growth there will be a concentration gradient in the liquid in front of the solidifying interface, where the interface concentration (C_L^*) is larger than the bulk concentration (C_0). If the concentration gradient causes the liquidus gradient to be higher than the temperature gradient in the melt, a zone of constitutional undercooling will exist in front of the solid/liquid interface. The liquid in this zone will therefore be at a temperature below its liquidus temperature. The constitutional undercooling (ΔT_c) can be calculated via the equation.

$$\Delta T_c = T_L - T^* = -m_L(C_L^* - C_0) \tag{5}$$

where m_L is the slope of the liquidus line and T_L is the liquidus temperature [42]. Newly formed solid grains in the melt will increase the energy of the system, due to the solid/liquid interface energy [42]. A curvature undercooling (ΔT_r) is then needed to overcome this increase in energy and drive further growth.

$$\Delta T_r = T_e - T_e^r = \frac{\sigma}{\Delta S_f} K = \Gamma K \tag{6}$$

where T_e and T_e^r are the equilibrium (melting) temperature of a flat surface and a sphere with

radius r, respectively. σ represents the solid-liquid interface energy, ΔS_f is the entropy of fusion, the curvature $K = \frac{1}{r}$ and the Gibbs Thomson coefficient $\Gamma = \sigma/\Delta S_f$.

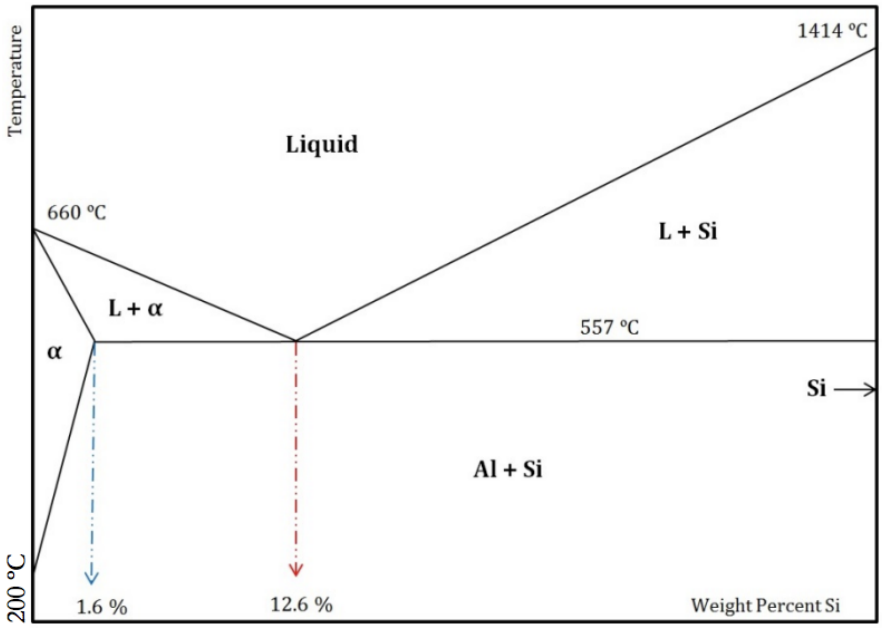

Figure 2.6: The aluminium rich part of the aluminium-silicon binary phase diagram [43].

As the solid-liquid interface is growing, local perturbations will form. The interface will remain planar if the perturbations does not survive. The condition for planar growth is:

$$\frac{G_L}{R} \geq -\frac{-m_L C_0(1-k)}{kD_L} \tag{7}$$

Where k is the partition coefficient between the solid and the liquid and D_L is diffusion coefficient of the solute in the liquid [42]. If the perturbations do survive, different growth morphologies can form. In pure metals the thermal field is the only source for growth, in alloys both thermal and solute forces drives growth [42]. The microstructures formed during solidification are' highly dependant on the solidification rate (R [m/s]) and thermal gradient (G_L[K/m]). While the cooling rate, i.e. the product G·R, determines the fineness of the microstructure [25]. As can be seen from figure 2.7 a planar interface interface is achieved at a low solidification rate and a steep thermal gradient. On the other hand, an equiaxed structure is created at high solidification rate and a lower thermal gradient. In a situation with a steep thermal gradient the zone of constitutional undercooling will be small. A small constitutional undercooled zone allows for little nucleation and the desirable equiaxed structure will be difficult to achieve.

As can be seen from figure 2.7 an increased cooling rate, i.e. $G \cdot R$, will result in a finer structure. Another approach to refining the structure is to add grain refining elements via various master alloys. Al-Ti-B are among the most effective master alloys for grain refining in aluminium alloys.

The amount of boron added is usually less than the amount of titanium and all of the boron will be bound to TiB_2. During the nucleation process the TiB_2 particles are evenly distributed in the liquid and the Al_3Ti particles dissolve. The excess titanium in the liquid that exists due to the dissolution of Al_3Ti creates a thin layer on the TiB_2 particles. This creates a very good heterogeneous nucleation site for α-aluminium. In addition to the nucleation effect the Al-Ti-B master alloy also has a solute effect that contributes to grain refinement. The segregation of solute Ti to solid/liquid interfaces slows down the growth of dendrites, it also increase the constitutional undercooling. An elements ability to hinder crystal growth during solidification is often measured by its' growth restriction factor(GRF) [13] [14]. The GRF is defined as:

$$Q = mC_0(k-1) \tag{8}$$

Titanium is one element with a high growth restriction factor.

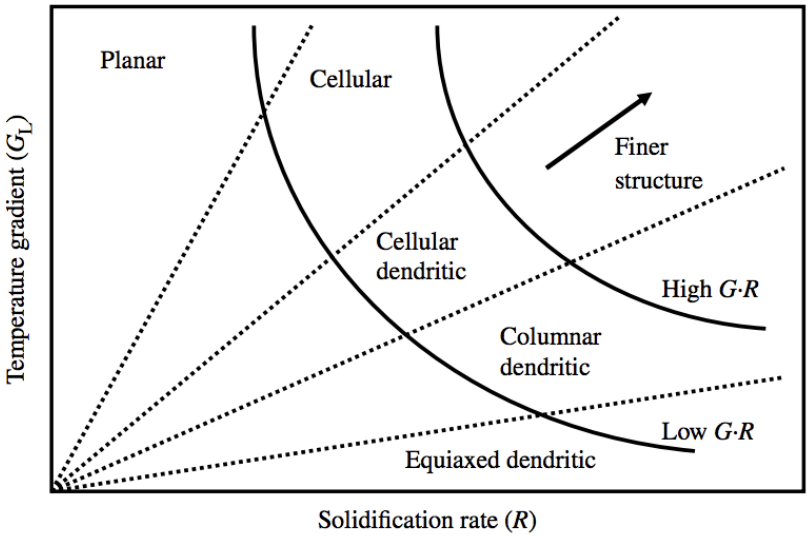

Figure 2.7: The influence of the thermal gradient and solidification rate on microstructure [44]

Cellular and and columnar dendritic growth begins as small perturbations in the solid-liquid interface. The tips of the perturbations can effectively reject solute, which will cause them to have an increased growth rate. Solute will accumulate in the space between growing perturbations and growth will therefore be hindered in these areas. During growth of columnar morphologies the melt is the hottest part of the system, G>0, this means that heat is conducted through the solid. For equiaxed growth the solid particles are the hottest part of the system, G<0, heat is then transported through the liquid which needs to be undercooled [34]. Dendrites are characterized by their primary dendrite arm spacing (λ_1) and their secondary dendrite arm spacing (λ_2). The secondary dendrite arm spacing (SDAS) is a function of the local solidification time (t_f):

$$\lambda_2 = 5.5(Mt_f)^{\frac{1}{3}} \tag{9}$$

Where M is a constant. The local solidification time is calculated via:

$$t_f = -\frac{\Delta T'}{\dot{T}} \tag{10}$$

Where $\Delta T' = m(C_l^* - C_l^m)$, C_l^m is the composition of the final liquid to solidify, $\dot{T}$ is the cooling rate. The negative value in equation 10 arises because $\dot{T}$ is negative. From equation 9 and 10 it becomes apparent that a more rapid cooling rate will lead to smaller SDAS compared to a slow cooling rate.

Due to more effective redistribution of solute a needle like tip will grow faster than a flat interface. The supersaturation, Ω, is the ratio of the concentration difference at the tip, ΔC, to the concentration difference according to the phase diagram, ΔC^*. I.e. $\Omega = \Delta C/\Delta C^*$. The supersaturation or the analogues constitutional undercooling represents the driving force for solute diffusion at a growing dendrite tip. The growth rate of new phases will increase with increasing supersaturation. The rate of rejection (and growth rate) is affected by the shape of the tip, simultaneously the distribution of heat and solute will influence the shape of the tip. This relationship makes an exact description very complex. However, if the tip is approximated to be a paraboloid the expression is simpler [34].

$$\Omega = I(P_c) = P_c exp(P_c) E_1(P_c) \tag{11}$$

Where P_c is the Peclet number. The Peclet number is the radius of the tip divided by the diffusion length.

$$P_c = \frac{R}{\frac{2D}{V}} = \frac{RV}{2D} \tag{12}$$

I(P) is the Ivanstov function and I(P) = P is a satisfactory approximation. This gives the following result:

$$P_c = \frac{RV}{2D} \approx \frac{C_l^* - C_0}{C_l^* - C_s^*} = \Omega \tag{13}$$

This simple solution describes the diffusion field surrounding a hemispherical cap.

The eutectic reaction, $L \rightarrow \alpha + \beta$, is an invariant reaction, which means it is a reaction with three components in equilibrium. This means, according to Gibbs' phase rule for constant pressure, that the reaction will happen at a constant temperature [11]. For aluminium, the eutectic temperature

is 557°C, which can be seen from the phase diagram in figure 2.6. Two phases, α and β will grow simultaneously during eutectic solidification. The two growing phases have very different chemical compositions; therefore, mass transport is a key driving force for growth. Component A will diffuse from β to α and component B will diffuse from α to β and the growth will be largely dependent on this diffusion [34]. To reduce the diffusion distance and therefore increase the growth rate, the eutectic distance λ will be minimised. This will, however, increase the curvature of the solid/liquid interface, which increases the demand for curvature undercooling. The point where α, β and the liquid meets the surface tensions needs to be in mechanical equilibrium. This means that the α/β interface energy needs to be balanced by the α/liquid and β/liquid interface energies [34]

In a situation with extremely rapid solidification, the equilibrium phase diagram is no longer valid, i.e. local equilibrium no longer exists at the solid/liquid interface. Also, the chemical potentials of the solid and liquid are no longer equal. The cause of rapid growth can be one of two things: high undercooling of the melt or a fast-moving temperature field. High undercooling can, for example, be achieved by quenching. While, fast-moving temperature fields occur with the use of a high-intensity heat source, like a laser or electron beam. The latter is the cause of the high growth rate in the selective laser melting process. If the growth rate, V, gets large enough, it will cause the partition coefficient, k, and the slope of the liquidus, m_L, to drift away from equilibrium values. If the growth rate is larger or comparable to the diffusion rate, D_i/δ_i, the solid crystal has no time to change its composition in order to reach the same chemical potential as the liquid melt. For very high growth rates, $V >> D_i/\delta_i$, re-arrangement of the atoms will not occur and solute atoms will be frozen into the solid. This phenomenon is called solute trapping. D_i is the interface diffusion coefficient, and δ_i is the distance between atomic planes. A consequence of the increased growth rate is that the composition of the solid and liquid at the interface will become more and more similar due to less time for diffusion. When the liquid interface composition, C_l^*, is equal to the solid interface composition, C_s^*, complete solid trapping has occurred. As mentioned above, rapid growth will cause the partition coefficient and the slope of the liquidus to no longer be at equilibrium values; new equations are therefore needed. The growth rate dependant partition coefficient, k_v, is written as:

$$k_v = \frac{k + (\delta_i V/D_i)}{1 + (\delta_i V/D_i)} \tag{14}$$

The growth rate dependant liquidus slope is:

$$m' = m[1 + f(k)] \tag{15}$$

where

$$f(k) = \frac{k - k_v[1 - ln(k_v/k)]}{1 - k} \tag{16}$$

At very high growth rates, complete solute trapping will occur ($C_l^* = C_s^*$), i.e. the concentration profile ahead of the solid/liquid interface will be flat. In this situation, $k_v = 1$, which means that the liquidus and solidus lines have merged and have become one line. This last section regarding rapid solidification is based on chapter seven in *Fundamentals of Solidification* by Dr. W. Kurz and Prof. David J. Fisher[34].

2.4 Scanning electron microscopy

A scanning electron microscope (SEM) produces images by scanning the surface of a specimen with a focused electron probe. A typical SEM setup is shown in part a) of figure 2.8. The cathode inside the electron gun is a wolfram filament, which usually operates at 2700 K and has a radius of 100 µm. The emitted electrons are accelerated by the cathode and focused with the magnetic lenses. The magnetic lenses include the condenser lens and the objective lens. The size of the electron beam is controlled by the condenser lens, which decides the resolution. While the objective lens focuses the beam before it hits the specimen [45].

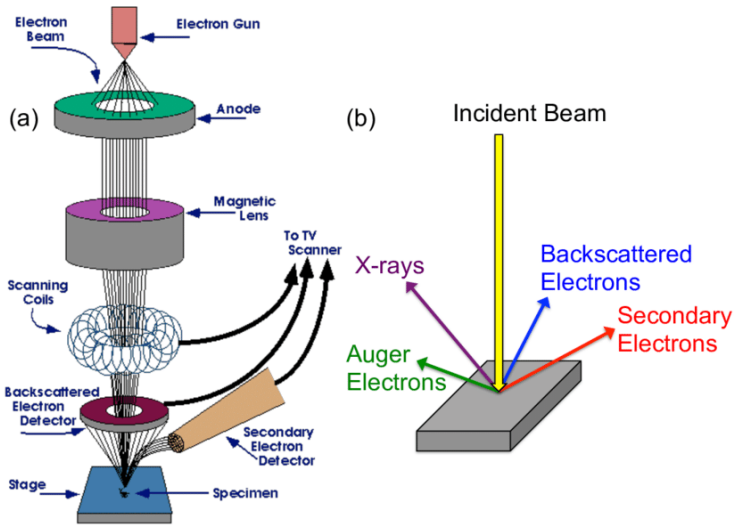

Figure 2.8: a) typical setup of the SEM, b) created signals in the SEM [46].

Once the electron beam hits the specimen, multiple signals are generated. These are backscattered electrons, secondary electrons, auger electrons and X-rays, which can be seen in part b) of figure 2.8. It has been found that a significant fraction of the primary electrons that hit the specimen escape. The escaping electrons are called backscattered electrons. The fraction of backscattered electrons depends on the atomic number, where high atomic numbers have the largest fraction of backscattered electrons. Since phases with a high average atomic number will backscatter more electrons, they will appear brighter on the screen. Backscattered electrons will escape the specimen after a single or a few elastic collisions, and they will therefore lose a small amount of their original energy. A large fraction of the escaping electrons have lost a large portion of their energy [45].

Emitted electrons with less than 50eV are defined as secondary electrons. Secondary electrons will come from very shallow depths due to their low energy. As the secondary electrons penetrate deeper into the specimen, the probability for these electrons to escape will decrease fast. The depth of backscattered electrons is around 100 times larger than the depth of secondary electrons. Their low emission depths make secondary electrons excellent at providing information about the specimen surface [45]. If incoming electrons have the right amount of energy, they can excite electrons in the specimen to another electron shell. When the electron falls back to its ground state, a characteristic X-ray may be created. Each element's characteristic X-ray will have a different energy, so these X-rays can be applied for elemental analysis [45].

Electron backscatter diffraction is a characterization technique used in SEM to gain information about the crystallographic orientation and the crystalline structure. The crystalline structure will affect how the primary electrons interact with the atoms. The orientation of the crystal structure will affect how deep the primary electrons will penetrate, this is because the structure is more open in certain directions. As mentioned above the probability for the electrons to escape decreases with the penetration depth, so the more open crystallographic orientations will emit fewer electrons [45]. This effect will create a pattern and Bragg's law can be used to indicate the different crystallographic planes. Since the crystallographic orientation is constant within a grain, the grain structure of the specimen surface can be characterized. However, it is important that the surface is well polished and without deformations [45].

3 Experimental

3.1 Remelting of deposited surface film with variation in composition

A surface film produced with physical vapour deposition was subjected to laser surface remelting. First a preliminary parameter test of a deposited surface was performed, then remelting of a film with aluminium, silicon and chromium was remelted, which is the alloy system studied in this work. The aluminium, silicon and chromium film has a large variance in chemical composition, meaning that many alloys are present in the film. Remelting of this film makes is possible to study several AlSiCr alloys after they have been subjected to conditions similar to those found in SLM. Proprieties of interest such as surface hardness, electrical conductivity and susceptibility for crack formation was mapped with regards to chemical composition.

3.1.1 Preliminary laser parameter test on 2 wt% copper alloy

Due to laser scanning of sputter-deposited surfaces being in its infancy, a preliminary parameter test was performed. This was done to gain knowledge on how this kind of surface would react to laser remelting, especially with regard to melt pool depths. The test sample consisted of a

base substrate, made of aluminium 6060 T6, with a deposited surface film with 2% copper and small amounts of titanium. The film was deposited with the technique that is shown in figure 3.2. The layout of the laser scanning is shown in figure 3.1 and the parameters used are shown in table 2. The SLM 280 from SLM Solutions was used for this re-melting and all of the following remeltings. The sample was cut into smaller pieces and the cross-section of the laser remelted lines was polished. The cross-sections were analyzed with Zeiss Ultra 55 scanning electron microscope (SEM), with a working distance of roughly 10 mm and an accelerating voltage of 10 kV. The depth of the remelted zone of each line was measured with the iSolution DT software and plotted against line energy.

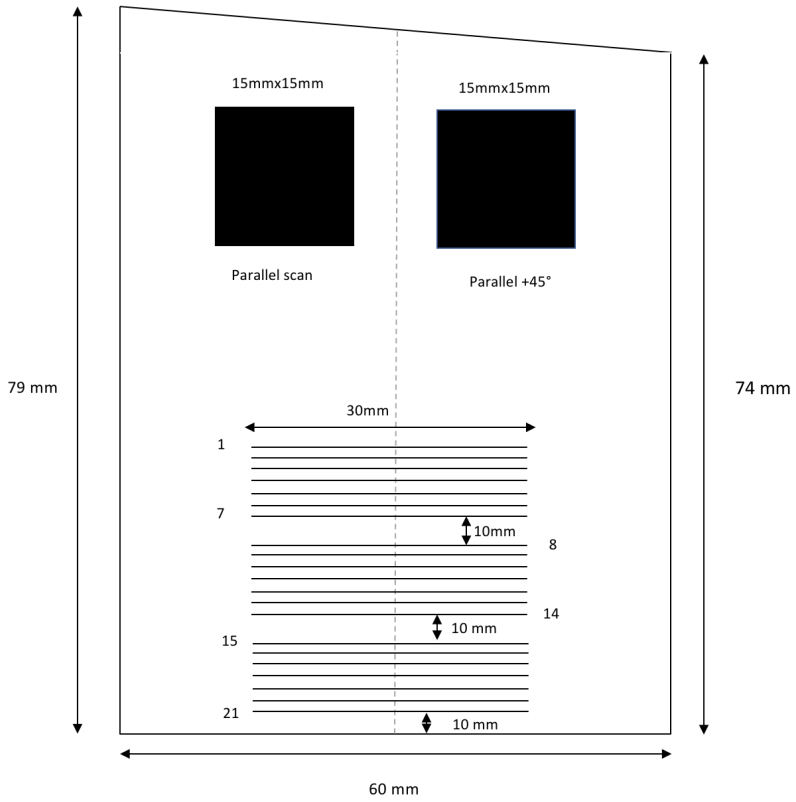

Figure 3.1: The layout of laser parameter test

Table 2: Laser parameters used in a preliminary test

Parameter	Laser power (W)	Scanning speed (mm/s)	Line energy (J/m)
1	200	500	400
2	200	750	266.7
3	200	1000	200
4	200	1250	160
5	200	1500	133.3
6	200	2000	100
7	200	2250	88.9
8	400	500	800
9	400	750	533.3
10	400	1000	400
11	400	1250	320
12	400	1500	266.7
13	400	1750	200
14	400	2000	177.8
15	200	2250	149.8
16	250	1335	187.3
17	300	1335	224.7
18	350	1335	262.2
19	370	1335	277.2
20	400	1335	299.6
21	450	1335	337.1

Based on the results from the preliminary parameter test, laser parameters for the AlSiCr system was chosen.

3.1.2 Laser surface remelting of aluminium-silicon-chromium alloy system

Three targets were used for the deposition process, 1050 aluminium (commercially pure aluminium), pure silicon and AlCr20. A film with a composition gradient is created on the substrate since the flux from each target will vary on the substrate surface, i.e. the part of the substrate plate that is closer to a certain target during the deposition will get a higher concentration of the element(s) of that target. For more details on the deposition process, the reader is referred to [47], by Leijon et al. The film was deposited onto a 6060 T6 aluminium substrate. Figure 3.2 shows the methodology from film deposition to laser re-melting and characterization. Since three sputtering targets have been used in this work, the gradient film consists of three elements instead of two, as shown in figure 3.2.

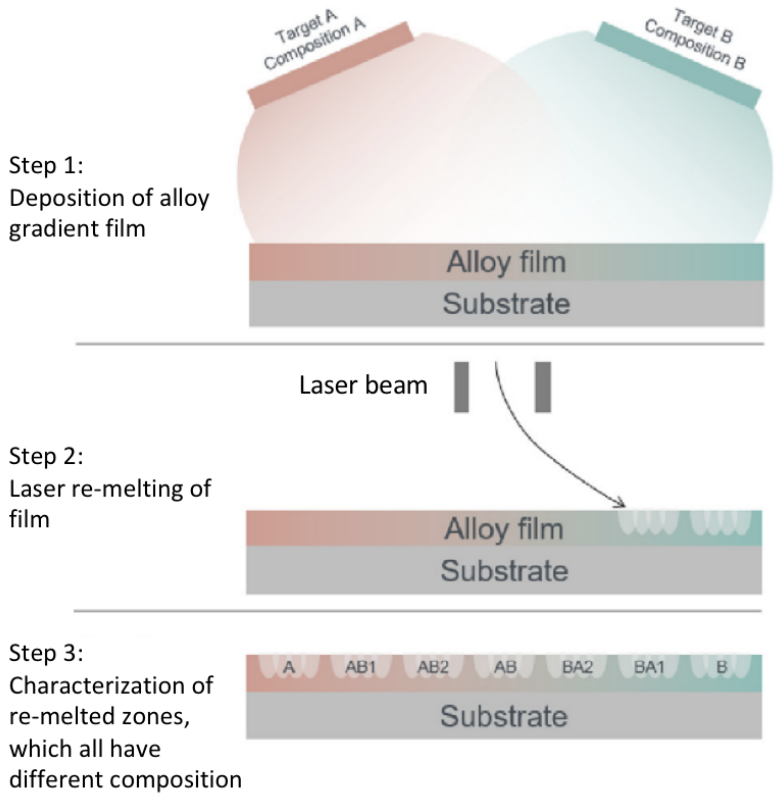

Figure 3.2: Deposition method and following laser remelting illustration [47].

The deposited AlSiCr-sample was received from Freddy Leijon from Linköping University. The plate was 60cm x 22cm and therefore needed to be cut to fit into the SLM machine. The plate was cut into three equal pieces. A small piece along the top of the plate was cut to check the thickness of the deposited film. To not damage the deposited film the plate was dry cut with a band saw, that is without any form of cooling liquid. The sample was also wrapped in plastic wrapping to protect the surface during cutting. The original plate was cut into three equal pieces of 20cm x 22cm, a top, middle and bottom part. Figure 3.3 shows COMSOL simulations of the film's concentration variation of silicon, chromium and aluminium. Figure 3.3 also shows how the film thickness is expected to vary on the plate surface. The dashed lines show where the plate was cut. The part of the plate with low chromium will hereby be called "top" and the part with high chromium will hereby be called "bottom", see figure 3.3.

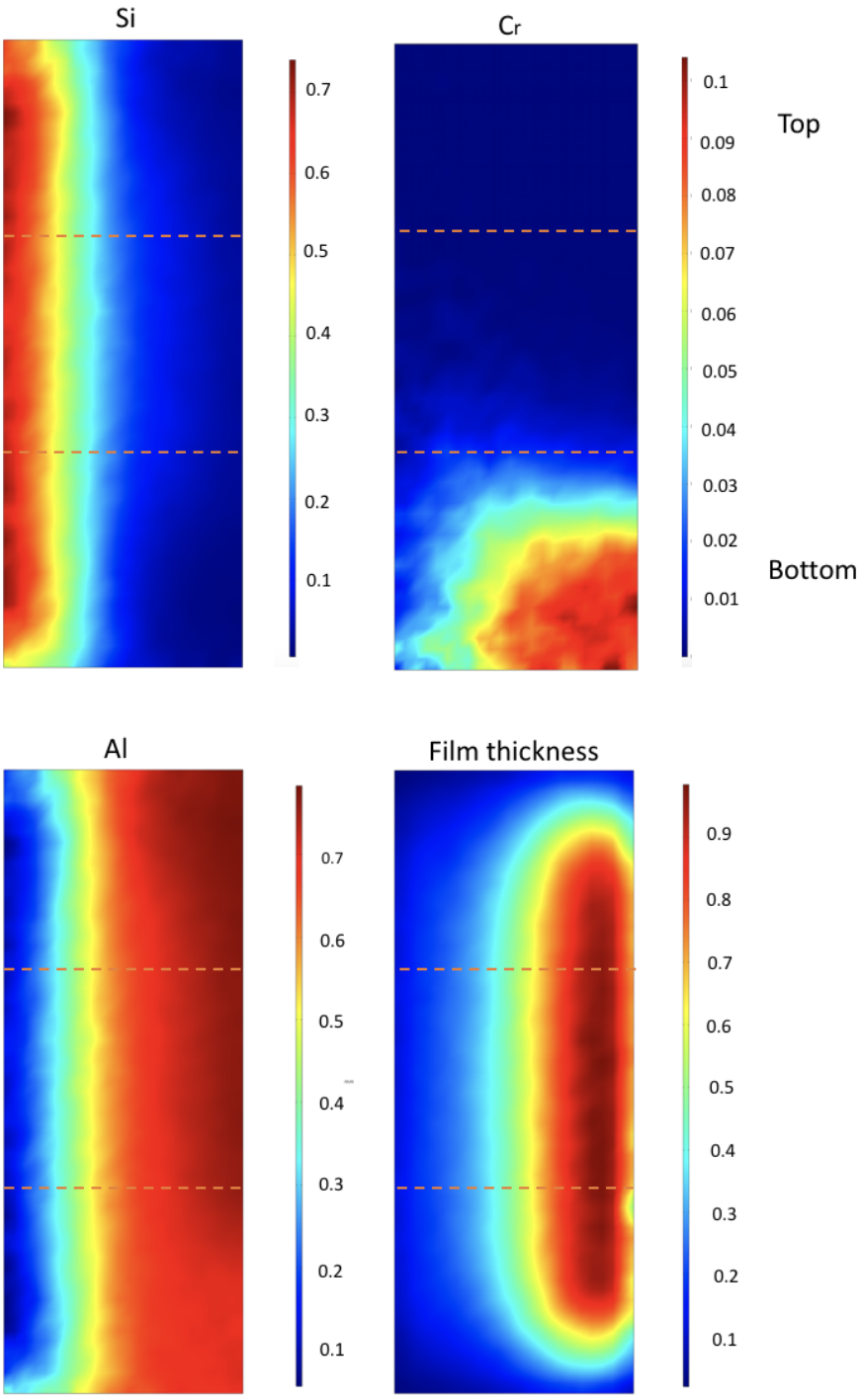

Figure 3.3: COMSOL simulations of film thickness and element distribution. The scale bar for the element distribution shows atomic fraction, while the one regarding film thickness is a relative scale, where 1.0 is 200 µm.

The top part of the plate was remelted as shown in figure 3.4. A combination of area remelting and line scan was performed. Four sections of 8 lines with different laser parameters were scanned on different areas along the top of the sample. Since there is a composition gradient film on the surface, each section of 8 lines was scanned on an area with different composition.

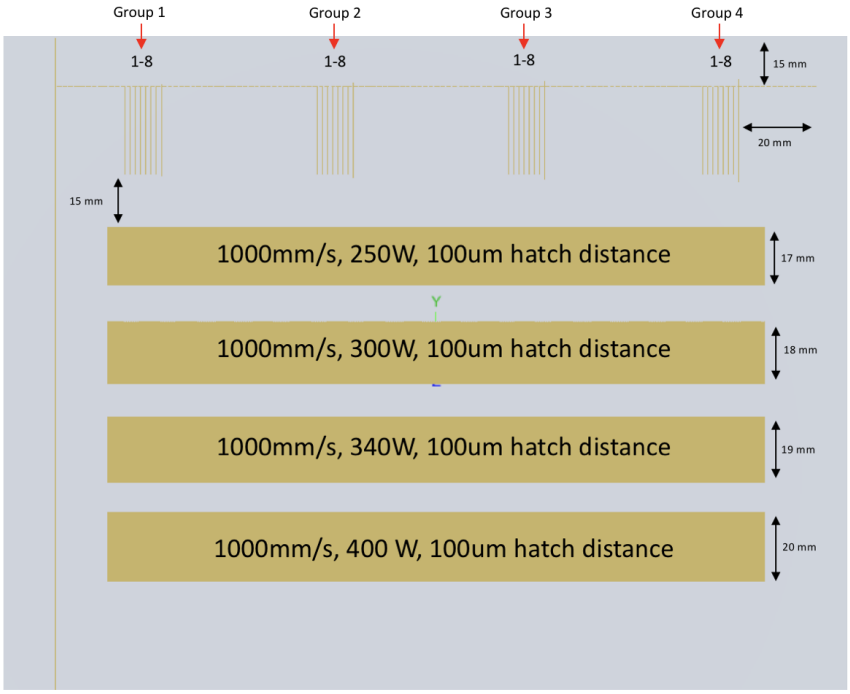

Figure 3.4: The layout of laser scanning of the top part of the AlSiCr-plate. The numbers 1-8 represents laser parameters 1 through 8, not to be confused with parameter 1-8 in table 2

Table 3: Laser parameters used for line scanning of top part of AlSiCr-plate

Parameter	Laser power (W)	Scanning speed (mm/s)
1	200	1000
2	250	1000
3	300	1000
4	350	1000
5	375	1000
6	400	1000
7	425	1000
8	450	1000

A remelted surface is expected to be more resilient than the original deposited surface. Saws with cooling water, Struers Accutom-5 and Struers Labotom-5, were used to cut the plate in order investigate the cross-section of the remelted lines. However, a dry cut was performed with a band saw to separate the section of remelted lines from the section of remelted areas. This was done to hinder the cooling liquid from doing any alterations to the remelted surfaces. Four samples, one for each group 1-4 (see figure 3.4), were mounted in epoxy and polished with Struers Tegramin-30. To minimize the charging effect in the SEM, the epoxy mounted samples were wrapped in aluminium

foil and coated with a thin layer of conductive carbon using the Cressington Carbon Coater 208. Energy-dispersive X-ray spectroscopy (EDS) was used to measure the chemical composition of the film in un-scanned areas and for some of the scanned lines. The composition was measured in remelted zones that had penetrated the surface film and in a melt pool where penetration did not occur.

The film thickness was measured in four spots on the lower part of the top part of the AlSiCr plate, one at each side and two evenly distributed between them. The thickness at the left and right sides was 38 µm and 165 µm, respectively. While the thickness in the two middle sites was 64 µm and 110 µm. Based on the results from the remelting of the top part of the AlSiCr and the thickness measurements, remelting was performed with a laser power of 200 W and a scanning speed of 1000 mm/s, resulting in a line energy of 200 J/m. These parameters were chosen to try to avoid penetration of the film by the laser created melt pools.

Figure 3.5: The layout of laser scanning of the bottom AlSiCr plate. All areas were scanned with 200 W laser power, 1000 mm/s scanning speed and 80 µm hatch distance.

Electrical conductivity measurements were performed on the remelted surface, using Sigmatest 2.069. Measurements were performed on points with a 1 cm distance between each point. A frequency of 960 kHz was used, which is the highest frequency available on the instrument. A high frequency will make sure the electrical conductivity is measured in shallower depths, a high frequency was therefore used in an attempt to avoid the measurement depth exceeding the thickness of the film.

Vickers hardness test were performed on the remelted areas of the bottom part of the AlSiCr plate, with a load of 500 g. Struers Duramin-40, which has a motorized stage was used for the

measurements. For each of the eight remelted areas, see figure 3.5, 3 lines of 22 indent points were taken. The instrument is intended for automatic indentation and measurement, but due to the roughness of the surface each point had to be measured manually.

SEM pictures and EDS measurement were taken with Zeiss Sigma 300 VP, in a grid with 1 cm spacing between points. Each picture was checked for cracks, in order to find out which chemical compositions produced cracks.

Backscatter electron (BSE) images were taken of the cross section using SEM Zeiss Ultra 55. Due to problems with the accelerating voltage and working distance with the SEM at this time, the results show inconsistent working distance and accelerating voltage. The display did not show correct working distance, so this needed to approximated by eye while being in the camera mode. EDS measurements were taken on each sample after BSE images.

3.2 Development of aluminium-silicon-copper alloy by wedge casting and laser surface remelting

.

By using A356 aluminium as the base alloy two alloys were designed and cast in a wedge-shaped copper mould. Pure titanium and pure copper were added, while the master alloys Al-20Mn, Al-5.8Zr and Al-14.6Cr were added to reach the desired level of manganese, zirconium and chromium, respectively. The composition of the two alloys is shown in table 4. These alloy compositions were chosen with the goal to achieve a combination of high strength and fine equiaxed grain structure after SLM. The clay crucible was coated with boron nitride lubricoat, was left to dry in a resitance furnace as it was heating up. The temperature of the furnace was set to 850 °C. The base alloy was added first, and the master alloys and alloying elements were added once the base alloy had been melted. The liquid aluminium was degassed before being cast in the wedge copper mould.

Table 4: Chemical composition of cast alloys.

	Si (wt%)	Cu (wt%)	Mn (wt%)	Zr (wt%)	Ti (wt%)	Cr (wt%)
Alloy A	7	6.5	0.5	0.2	0.1	0.2
Alloy B	7	6.5	0.5	0.2	0.8	0.2

Three samples with different thickness were cut from the wedge cast for each alloy. One thick part from the top, one middle part and one thin part from the wedge tip. The samples were polished with Struers Tegramin-30 using different polishing cloths and lubricants, further the samples were anodised with Struers LectroPol-5 with a diluted HBF_4 electrolyte for 90 seconds with a voltage of 20. Optical microscope (OM) pictures were taken using polarised light to identify the different grains.

The wedge mould is shaped so that on one side at the tip a thin flat plate is created, this is done to easily create a flat laying sample from the tip. This part was cut off from the rest of the and subjected to laser scanning to cause surface remelting. 46 lines with different laser parameters and two areas with different scanning strategies were scanned. A preheating temperature of 200 °C was used. The layout of the scanning is shown in figure 3.6. A laser power of 370W, scanning speed of 1335 mm/s and a hatch distance of 170 µm were used to scan the two areas (A1 and A2). A1 was scanned once with parallel lines, while A2 also were scanned a second time with same parameters, but with a 45 degree angle to the first scan.

The sample was cut perpendicular to the scanned lines to expose the cross-section of the remelted zone. The samples were then polished with SiC paper with water lubricant and various polishing cloths with diamond containing lubricants.

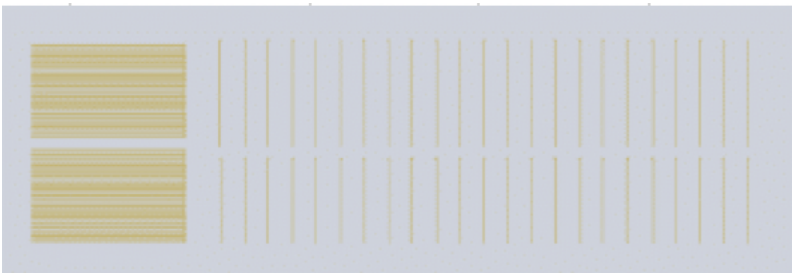

Figure 3.6: Layout of the laser surface remelting of the wegde cast tip

SEM pictures were taken of the cross-section of every line and, the working distance in the SEM was set to approximately 10mm and the accelerating voltage to 10 kV. The iSolution DT software was used to measure the depth of each remelted line, as well as the secondary dendrite arm spacing of both the remelted zone and the bulk material.

A1 on both samples, as well as one remelted line on alloy B, were analyzed in more detail with electron backscatter diffraction (EBSD). EBSD was performed with a working distance of 25 mm, accelerating voltage of 20 kV and 300 µm aperture. The samples were also tilted 70 °to allow for more electrons to be reflected from the sample to the EBSD detector. Since the EBSD technique is sensitive to the condition of the surface, the samples were ion milled for 30 minutes with an IM-3000 flat milling system, in order to improve the surface quality.

Innovatest were used to measure the hardness in the remelted zone and in the bulk area. Five measurements were taken in the bulk material and in the remelted zone of both alloys. A small load of 100g were used since the remelted zones are limited in size and a large load could make an indention bigger than the remelted zone itself.

4 Results

4.1 Laser scanning of deposited surface films

4.1.1 Preliminary laser parameter test

Figure 4.1 shows melt pool depth of Al-Cu-Ti test sample plotted against line energy of different laser parameters 8-21, from table 2. As can be seen the melt pool depth increases with increasing line energy.

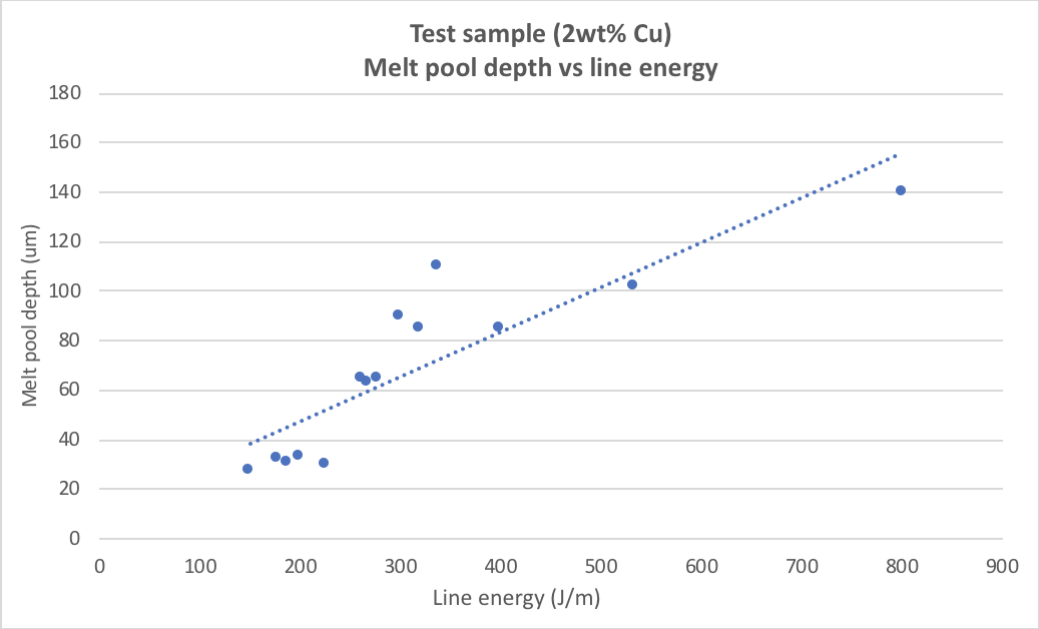

Figure 4.1: Melt pool depth vs line energy for parameters 8-21 on the test sample.

4.1.2 Laser scanning of top AlSiCr plate with low chromium content

Figure show 4.2 SEM-images of remelted cross section caused by laser scanning with parameter 1 from table 3 (200W, 1000 mm/s), for all four groups. It can be seen that the film on the surface has been penetrated in groups 1-3 and that the line scan in group 4 did not penetrated the film. Several big pores were present in the remelted zone, or in the vicinity of it. This was also the case for the lines shown in figure 4.4 and in several other scanned lines. The film thickness in figure 4.2 a),b) and c) is approximately 20 µm, while for d) the film thickness is about 40 µm.

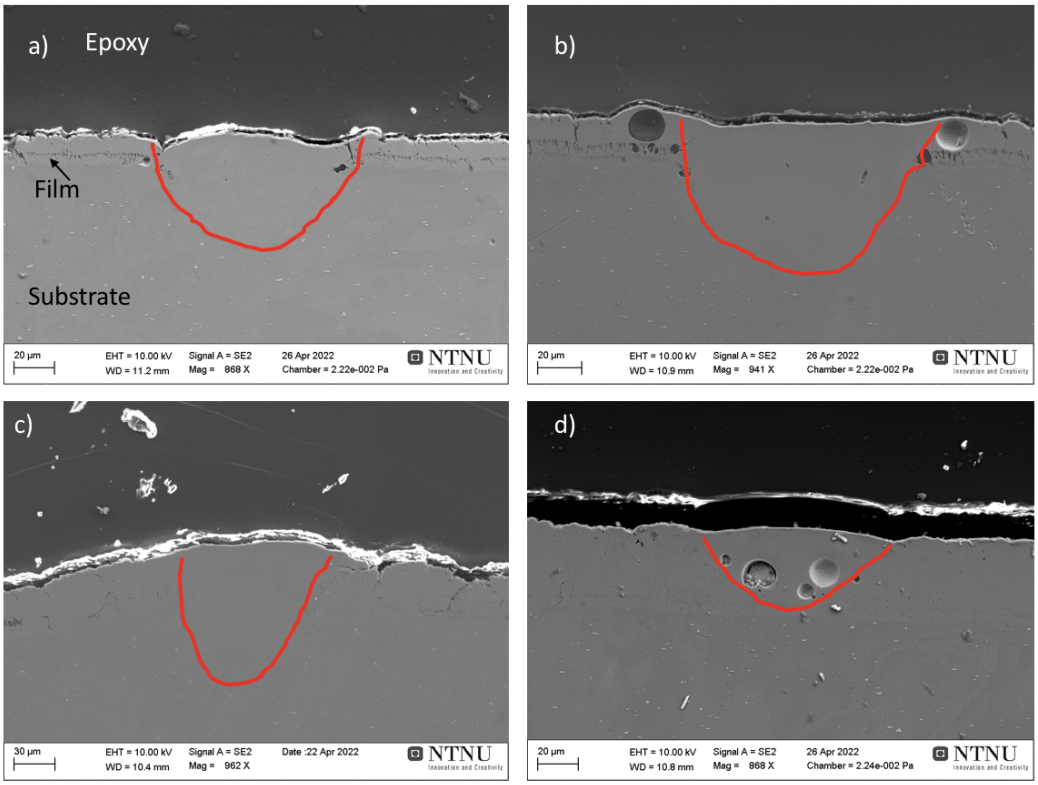

Figure 4.2: Cross-section of the remelted line from the top part of AlSiCr-plate. Scanned with parameter 1 (200W, 1000 mm/s), group 1-4 (picture a-d, respectively). The red lines represent the shape of the remelted zones.

Since the group of lines stretch out over a relatively narrow area, the film composition is assumed to be uniform within each group. The EDS measurements showed that group 1 had a film with 34.1 wt% Si, group 2 had 20 wt% Si, group 3 had 8.9 wt% Si and group 4 had 4.1 wt% Si. The silicon content in the penetrated melt pools was significantly lower, to the original content in the deposited film. While, the remelted line that did not penetrate the film had a similar chemical composition, compared to the original deposited film. Three points were measured in each of the selected remelted zones, similar to what is shown in figure 4.3. The EDS results are summarised in table 5, where it can be seen that some of the penetrated melt pools also had small amounts of magnesium. The Mg content is from the substrate alloy, aluminium 6060.

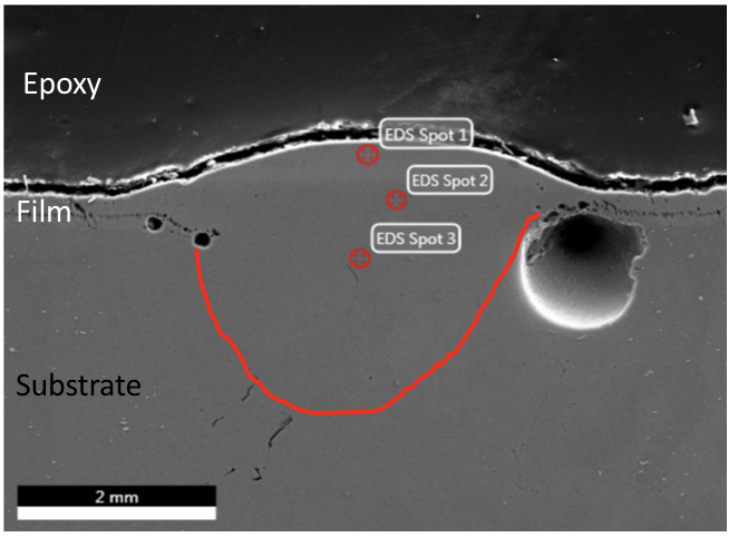

Figure 4.3: Example of spots where EDS was performed in a remelted zone that penetrated the film. Line 8 from group 1.

Table 5: EDS results of selected remelted lines in groups 1-4. Group 1-4 represents different locations on the plate, with different composition, see figure 3.4

Group	Scanning speed (mm/s)	Laser power (W)	Spot	Si(wt%) after RM	Mg (wt%) after RM	Original film composition (wt%Si)	Penetrated
1	1000	200	1 2 3	3.8 2.7 3.3		34.1	Yes
2	1000	200	1 2 3	4.6 1.6 2.5	1.31 1.3	20	Yes
3	1000	200	1 2 3	2.8 0.94 2.33		8.9	Yes
4	1000	300	1 2 3	0.87 1.85 3.52	1.32	4.1	Yes
4	1000	200	1 2 3	3.99 4.87 5.2		4.1	No

Of the total 24 lines scanned on the top part of the AlSiCr-plate, cracks were observed in four of the remelted zones. The cracks occurred in lines scanned with parameters 6, 7 or 8, i.e. the laser parameters with the highest power. The cracks were also only observed in groups 3 and 4 and they are all perpendicular to the scanning direction.

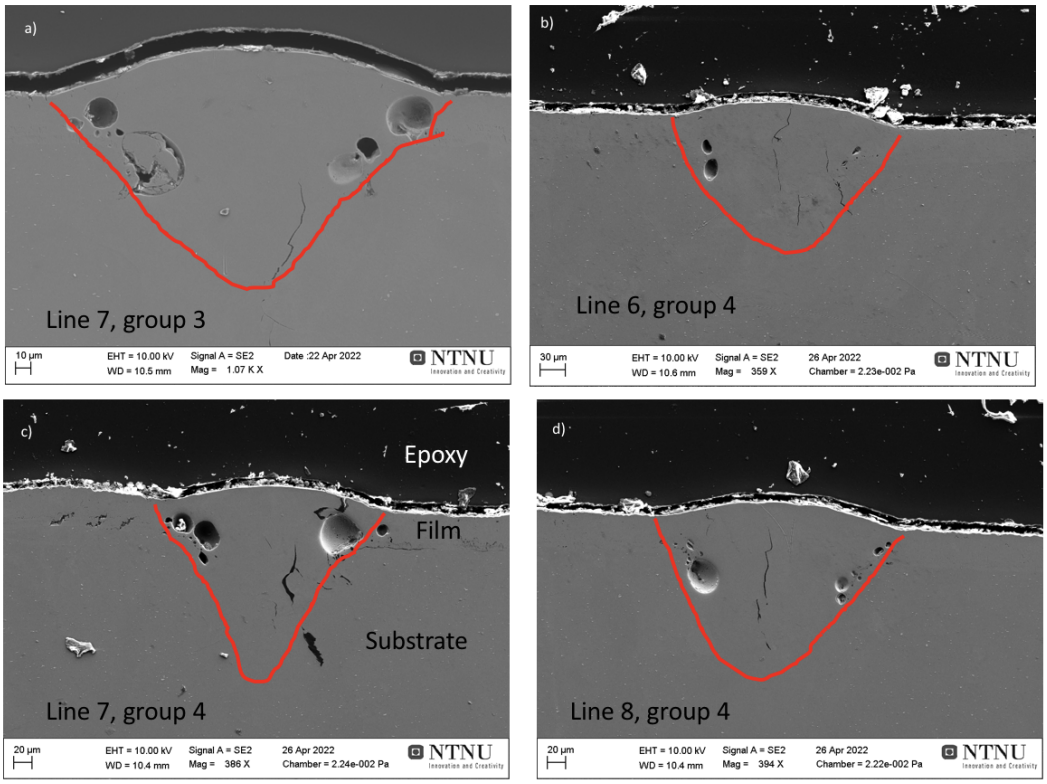

Figure 4.4: Cracks in the cross section of the remelted zone.

Figure 4.5 shows the depth of remelted zones versus the line energy. An approximately linear relationship is observed between the remelted depth and the line energy, where higher line energy leads to a deeper remelted zone. The plot also shows that each parameter produces a different melt pool depth depending on which groups it belongs to, i.e. where on the plate it was scanned. The deepest melt pools were consistently created in group 3 and the shallowest melt pools were often observed in group 1.

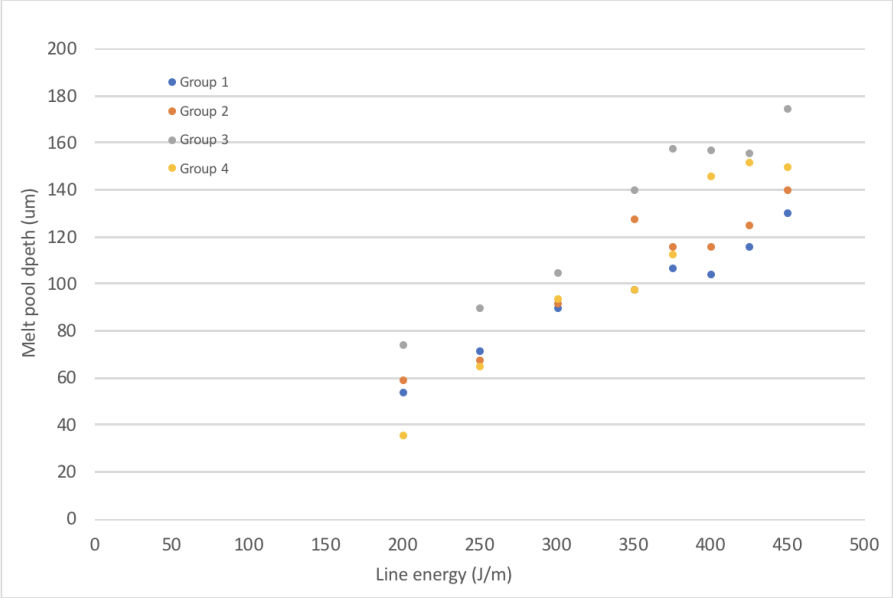

Figure 4.5: Melt pool depths plotted against line energy, for the lines in groups 1-4 in the top part of the AlSiCr-plate.

4.1.3 Laser scanning of bottom AlSiCr plate with high chromium content

The bottom plate after remelting is shown in figure 4.6. The remelted surface is shiny on the left side and black and matt on the right side. A mark can be seen on the remelted surface in the bottom left corner of the plate. Light optical microscope pictures of both the shiny and matt surface are shown in figure 4.7. The individual lines can be seen in both pictures, but they are easier to distinguish in picture b), in picture a) the lines are covered with a black substance. The surface looked almost burnt and when washed with a wet cotton stick, the cotton stick turned completely black.

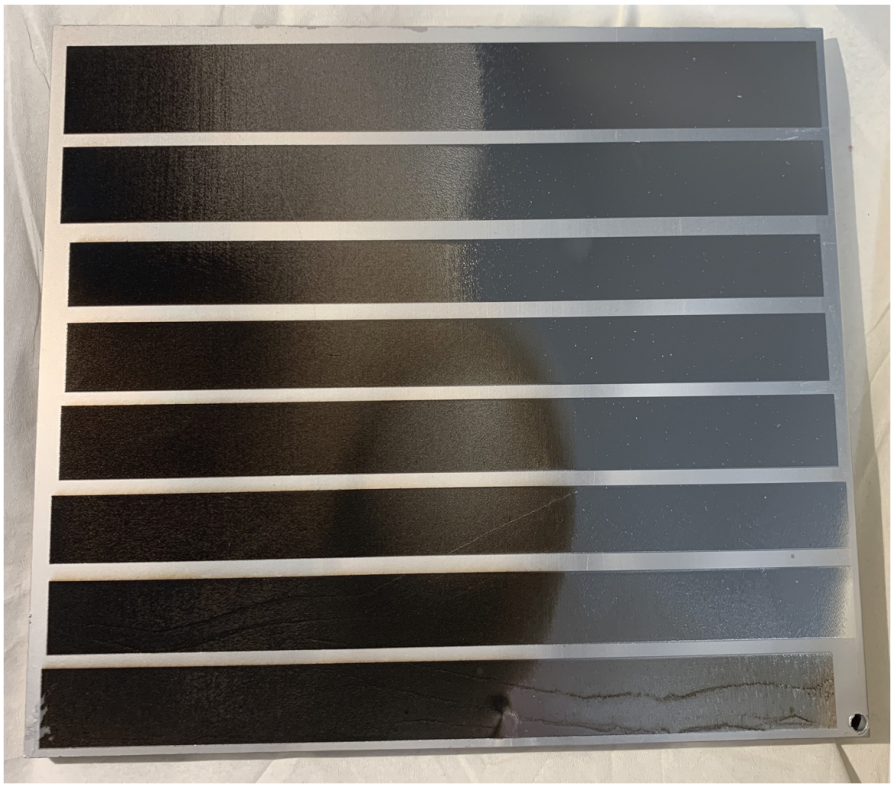

Figure 4.6: The bottom part of the AlSiCr plate after laser surface remelting

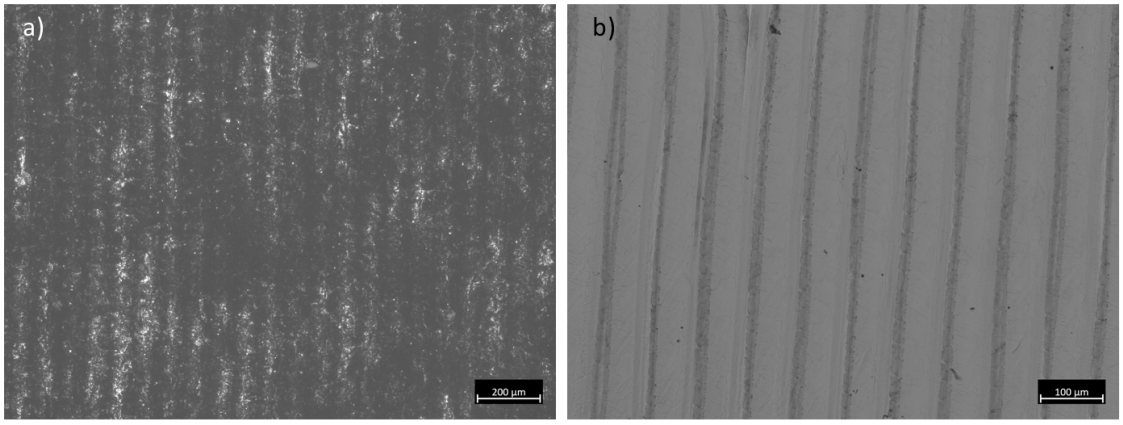

Figure 4.7: Remelted surface. Matt and black surface in picture a), shiny surface in picture b).

There was no significant difference between the morphology of the film across the surface. Figure 4.8 shows two examples of the film and where on the plate the pictures were taken. Both positions had a film consisting of fine spherical particles, which is due to the nature of the physical vapour deposition process. During depositon

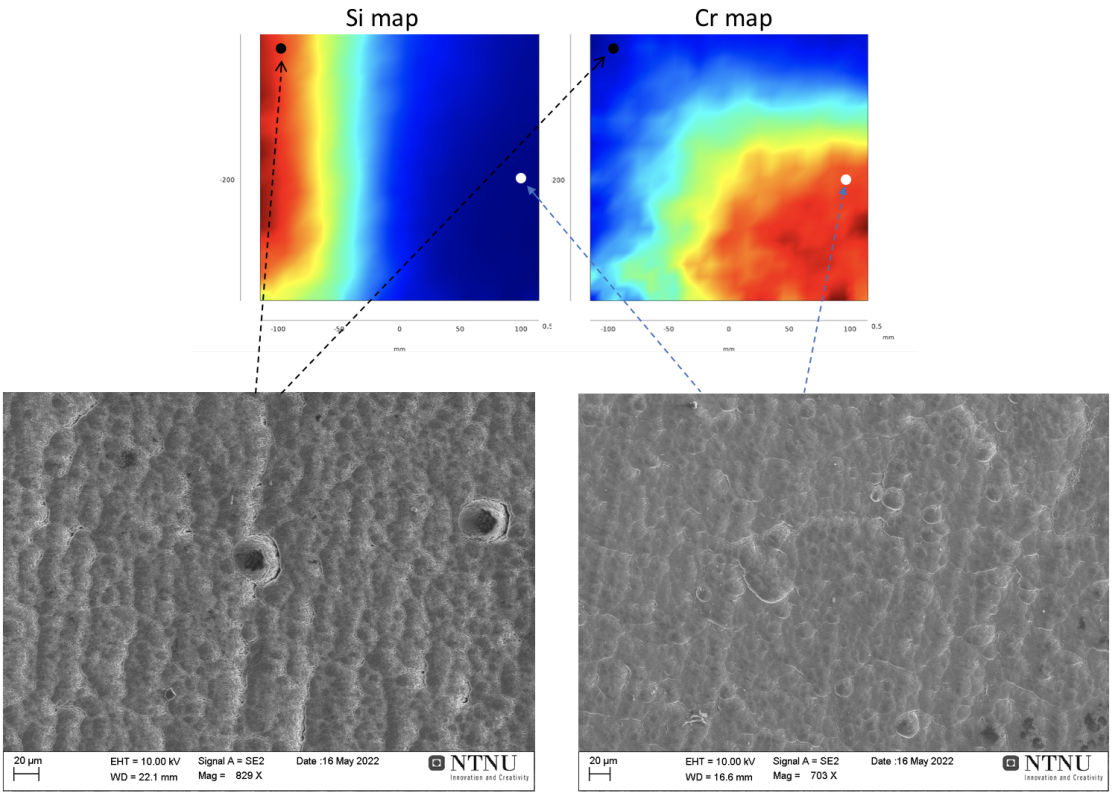

Figure 4.8: Morphology of the surface film in two different locations

Figure 4.9 shows the measured electrical conductivity of the remelted surface of the bottom plate in the format of a heat map. The lowest electrical conductivity was measured in the top right corner of the bottom plate where the content of both Si and Cr is low, while the highest electrical conductivity was measured along the bottom and along the right side where the Si content is high. In the figure the read areas have the lowest measured conductivity and the green areas have the highest measured condutivity. The lowest value measured was 9.977 MS/m, while the highest value was 26.48 MS/m.

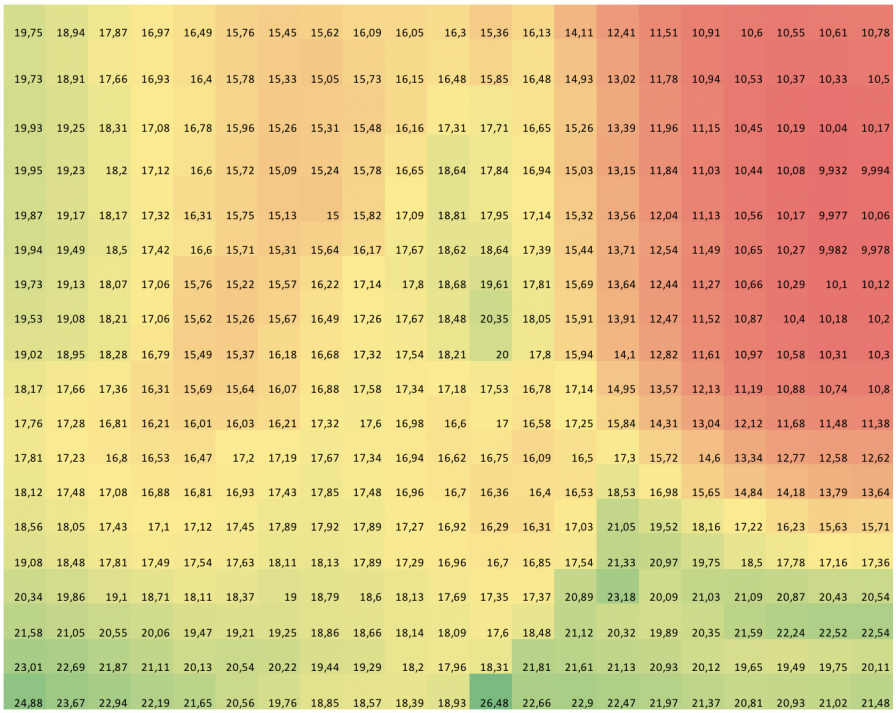

Figure 4.9: Electrical conductivity heat map of the bottom part of the AlSiCr plate. Conductivity values are in MS/m.

Figure 4.10 shows a heat map of the measured hardness values, the color green represent lower hardness values and red higher hardness values. The white space between the measurements represents the areas that were not remelted and hardness was therefore not measured in these areas. It can be seen that highest hardness values were measured in the top left corner and the lowest values in the top right corner, which is the area with high silicon, meaning that the the high silicon alloys had the highest hardness.

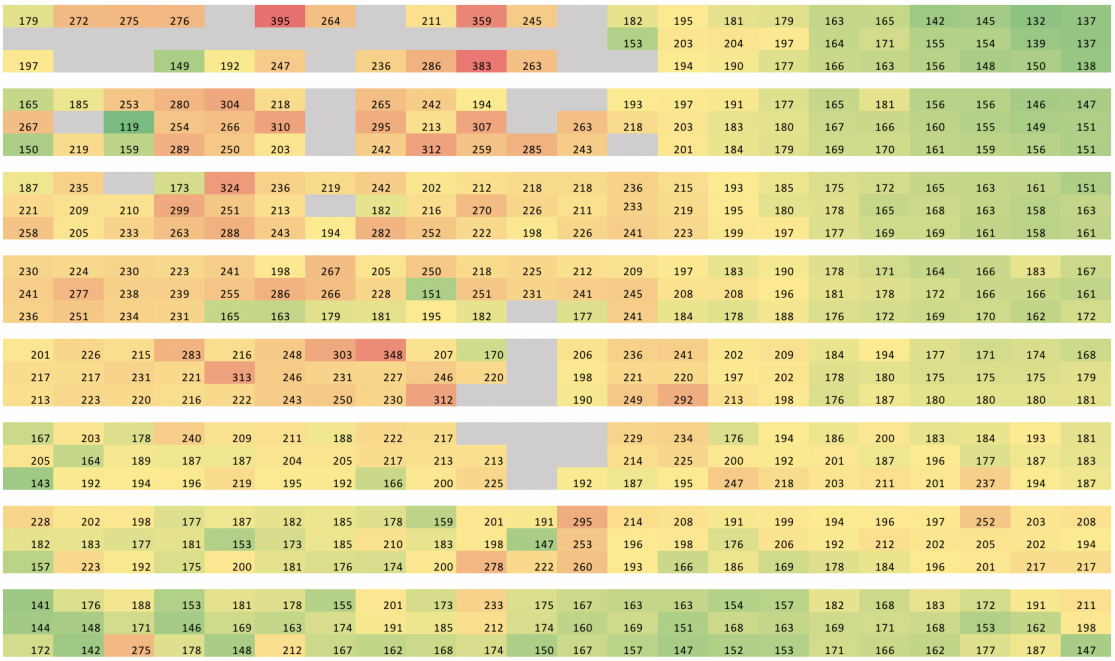

Figure 4.10: Hardness heat map of the bottom part of the AlSiCr plate. Values are Vickers hardness with a load of 500 g and indent time of 10 seconds. Grey areas represent areas where hardness value was not measured, due to missing indent or other errors.

Due to the difference in surface roughness across the plate, the size of the indents were significantly easier to identify in the shiny surface compared to the matt and black surface. An example of one indent from the matt and black surface and one indent from the shiny surface is shown in figure 4.11.

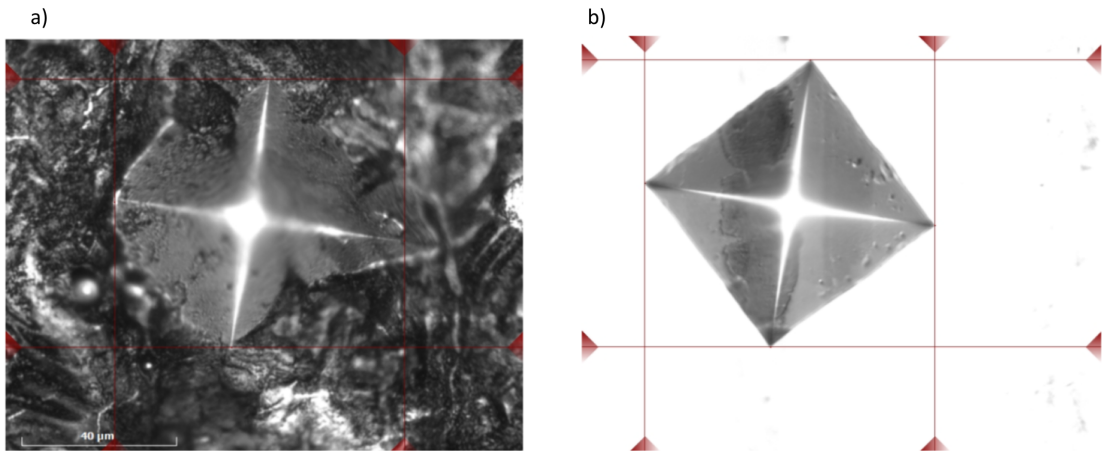

Figure 4.11: Example of hardness indentations from a) matt and black surface b) shiny surface.

The plot in figure 4.12 shows the combinations of silicon and chromium contents where surface cracks were detected and where surface cracks were absent. The compositions are measured with EDS analysis and cracks spotted from SEM pictures. Cracks were not detected in most of the

alloys. Cracks were mostly observed in alloys with a combination of silicon concentration between 10.6-12.5 wt% and chromium concentration between 2.3-4.3 wt%.

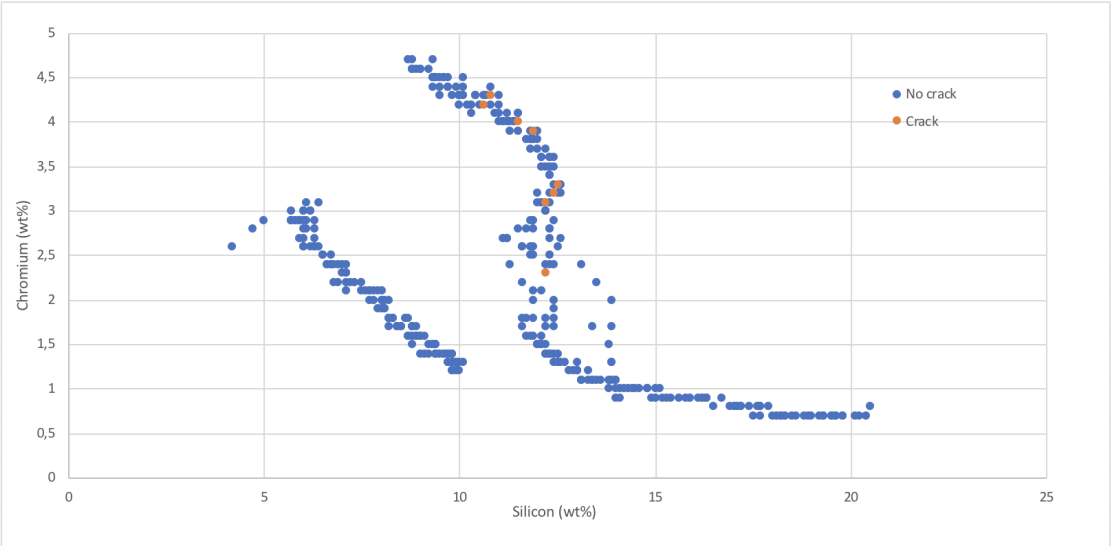

Figure 4.12: Observed surface cracks in relation to chemical composition.

Backscatter electron images of remelted cross section of the alloy with 12.6 wt% Si and 8.1 wt% Cr is shown in figure 4.13. No pores are present in the remelted structure, however pores are present in the boundary between the substrate and the remelted film.

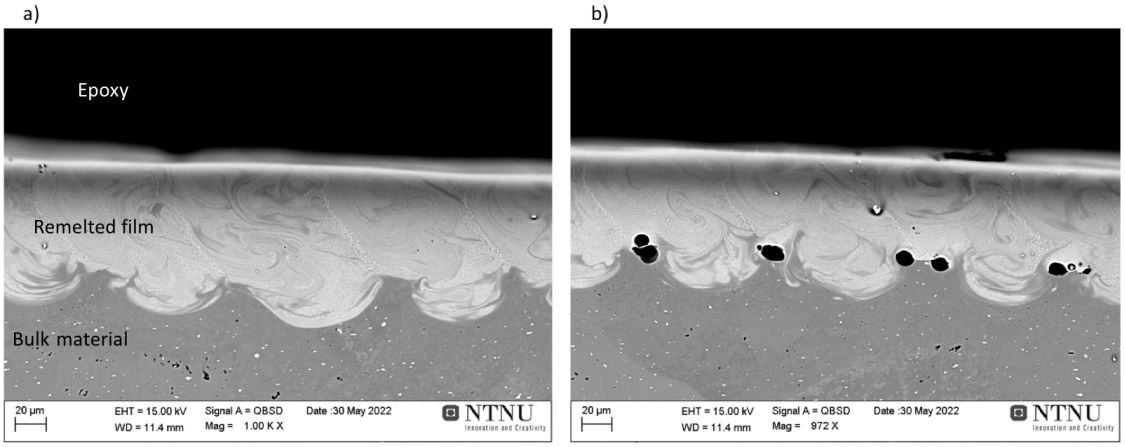

Figure 4.13: Backscatter electron image of remelted cross section. Composition: 12.6 wt% Si, 8.1 wt% Cr

Figure 4.14 shows SEM images with 15k and 25k magnification of the same sample as in figure 4.13, from approximately the center of the melt pool. It shows fine spherical particles evenly distributed in the microstructure, the particles vary in size roughly from 0.2 µm to 0.5 µm. The hardness of this microstructure was measured to be 190 $HV_{0.1}$.

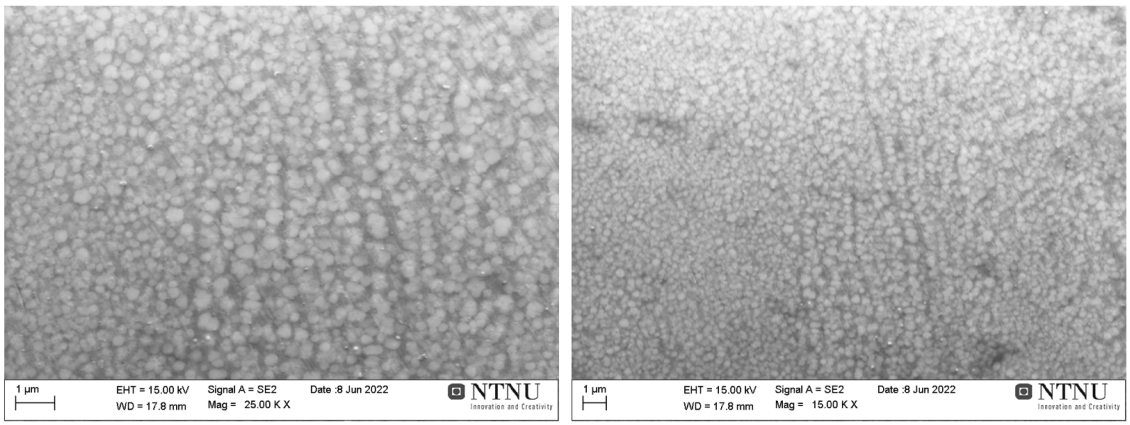

Figure 4.14: High magnification SEM-pictures of sample with 12.6 wt% Si and 8.1 wt% Cr.

Figure 4.15 shows backscatter electron image of remelted cross section of alloy with 9.9 wt% Si and 10.6 wt% Cr. It can be seen that melt pool penetrated the film in some positions and that in other positions the film was not penetrated. From a) a crack stretching from the unmelted film and into the remelted zone can be observed. The film contains cracks that originates from the deposition process, as can be seen in figure 4.17. If the film is not completely molten the cracks can propagate from the film and into the remelted zone.

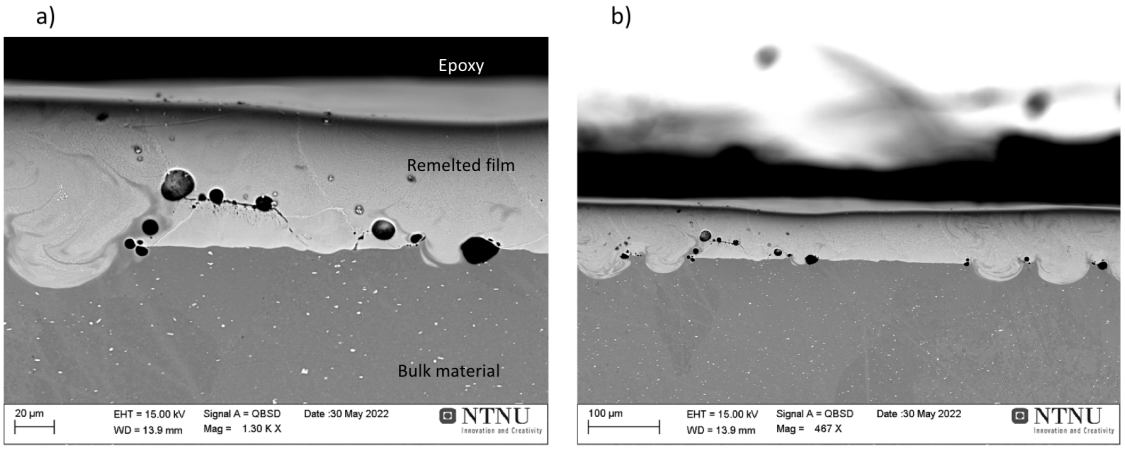

Figure 4.15: Backscatter elctron image of remelted cross section. Composition: 9.9 wt% Si, 10.6 wt% Cr

SEM images with 15k and 25k magnification can be seen in figure 4.16, from the center of the melt pool. The alloy is the same as is in figure 4.15. Similarly to the sample in figure 4.14, fine spherical particles are evenly distributed in the microstructure with a size ranging from 0.2 µm to 0.5 µm.

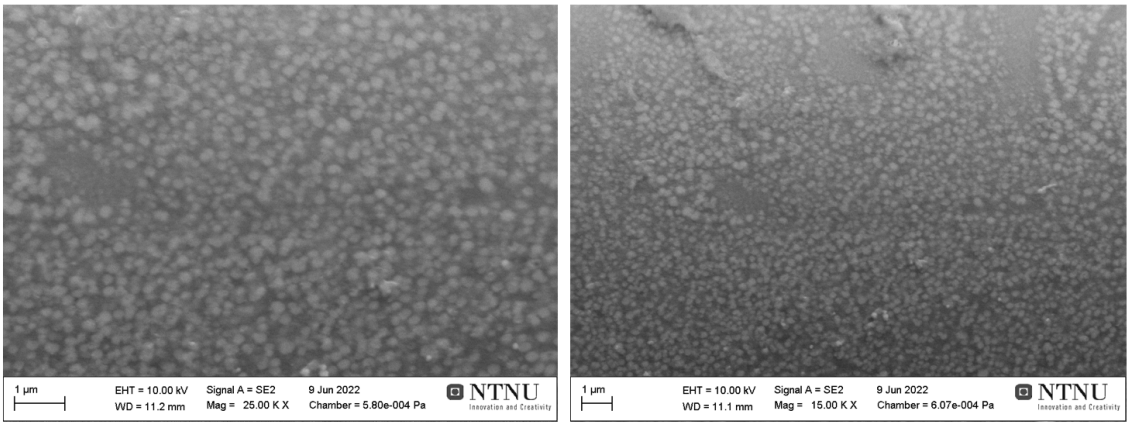

Figure 4.16: High magnification SEM-image of remelted cross section. Composition: 9.9 wt% Si, 10.6 wt% Cr

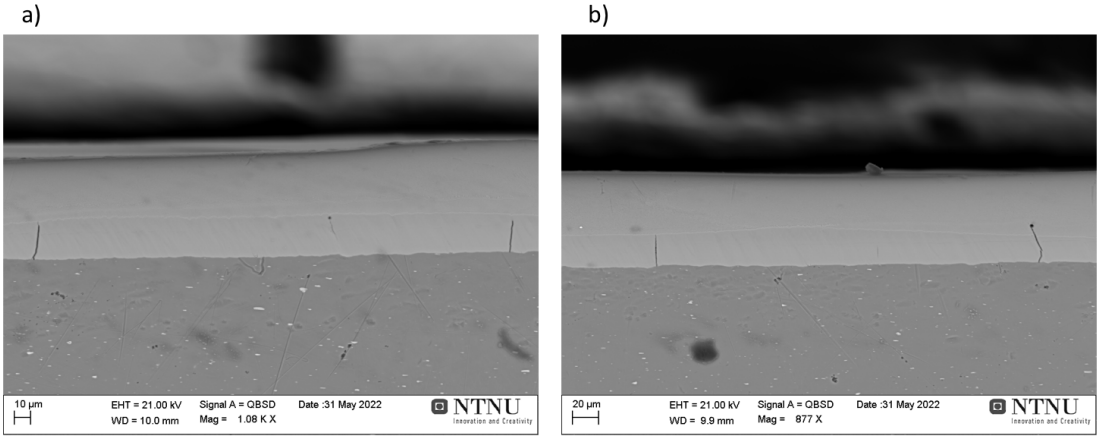

Figure 4.17: Backscatter electron image of remelted cross section. Composition: 8.7 wt% Si, 14.4 wt% Cr

Figure 4.18 shows remelted cross section of alloy with 21 wt% Si and 0.9 wt% Cr. The melt pool has penetrated the film and the mixing between film and substrate can be observed. Small spherical pores are present and they are evenly distributed in the remelted zone.

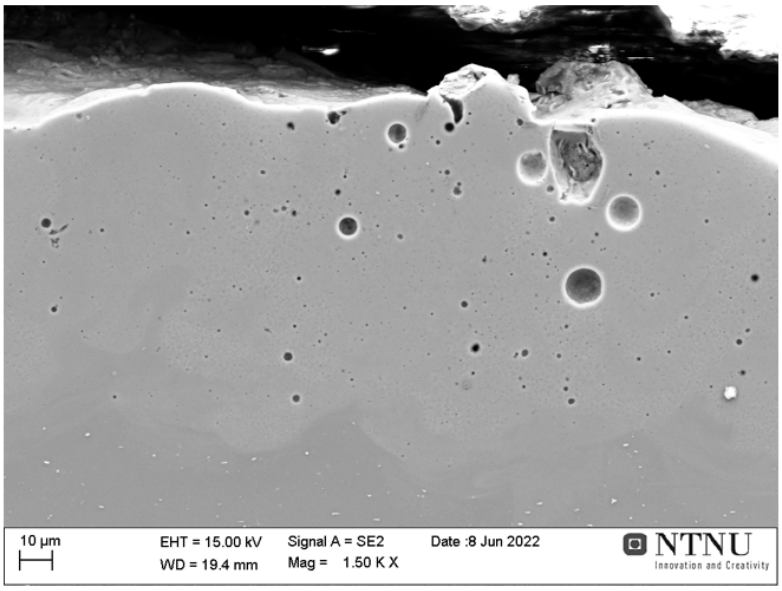

Figure 4.18: SEM image of remelted cross section of alloy with 21 wt% Si and 0.9 wt% Cr.

High magnification SEM images of the same alloy as in figure 4.18 with 25k and 40k magnification is shown in figure 4.19. A dendritic structure can be seen and the SDAS is approximately 0.45 µm. The black circles are pores and they vary in size from roughly 0.08 to 0.2 µm. The hardness of this alloy was measured to be 254 $HV_{0.1}$ in the remelted zone. Different from the alloys shown in figure 4.14 and 4.16, aluminium dendrite structure can clearly be seen. It can also be seen that the dendritic structure is more round and equiaxed than the structure in figure 4.21, which is more columnar.

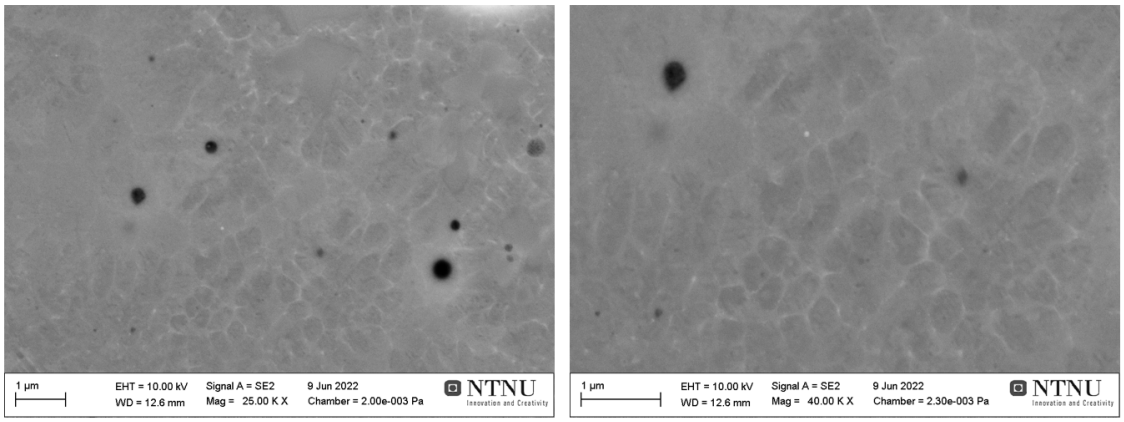

Figure 4.19: SEM images with 25k and 40k magnification of remelted cross section of alloy with 21 wt% Si and 0.9 wt% Cr.

The remelted cross section of an alloy with 15 wt% Si and 2 wt% Cr is shown in figure 4.20. The film has been penetrated and it is difficult to tell where the original boundary between film and substrate was. Both small and large spherical pores can be seen.

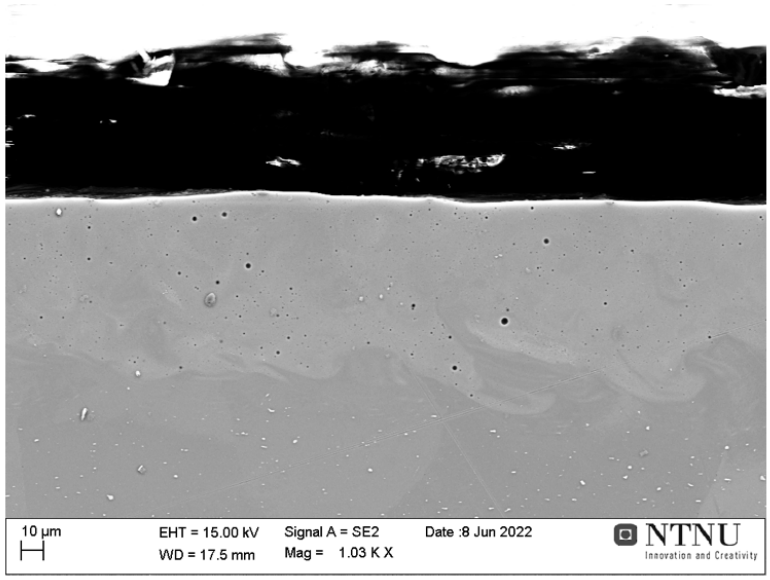

Figure 4.20: SEM image of remelted cross section of alloy with 15 wt% Si and 2 wt% Cr.

SEM images with 15k and 25k magnification of the alloy in figure 4.20 are shown in figure 4.21. The dendritic structure that can be observed has a SDAS of approximately 0.4 µm. In the interdentritic region are eutectic structures which are finer than in figure 4.19. Several pores can also be spotted in the structure with sizes roughly between 0.1 and 0.4 µm.

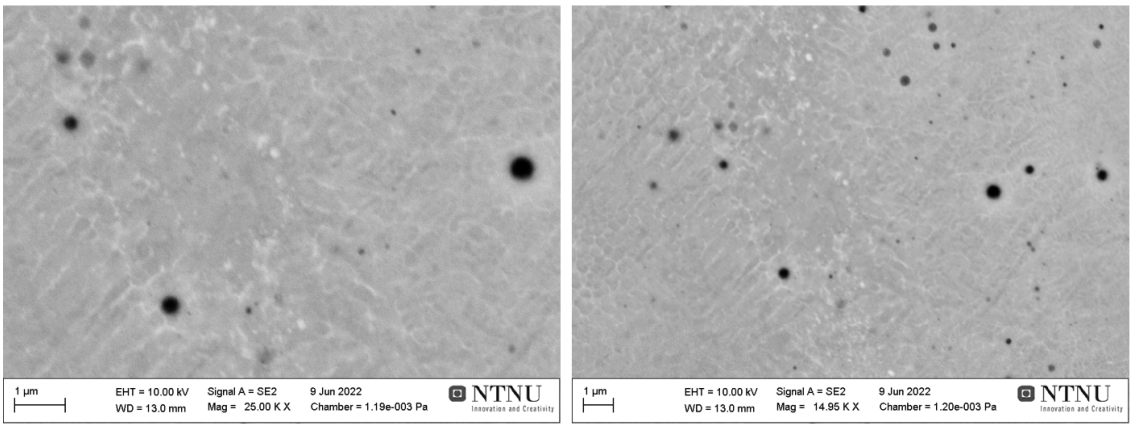

Figure 4.21: SEM images with 15k and 25k magnification of remelted cross section of alloy with 15 wt% Si and 2 wt% Cr.

Figure 4.22 and 4.23 show EDS measurements of pores and a crack found in the remelted zone and in the surface film. The measurements show that both the crack and pores have a high oxygen content. Oxygen content between 2.7 % and 8.5 % was measured in the crack and pores. No oxygen were measured in areas with no cracks or pores.

Spectrum: 35

Element	norm. C [wt.%]	Atom. C [at.%]	Error (3 Sigma) [wt.%]
Aluminium	65,59	67,49	5,00
Silicon	17,79	17,59	1,28
Chromium	11,59	6,19	0,63
Oxygen	5,03	8,73	1,21
Total:	100,00	100,00	

Spectrum: 31

Element	norm. C [wt.%]	Atom. C [at.%]	Error (3 Sigma) [wt.%]
Aluminium	68,73	72,27	4,20
Silicon	15,93	16,09	0,94
Oxygen	2,67	4,73	0,63
Chromium	12,67	6,91	0,56
Total:	100,00	100,00	

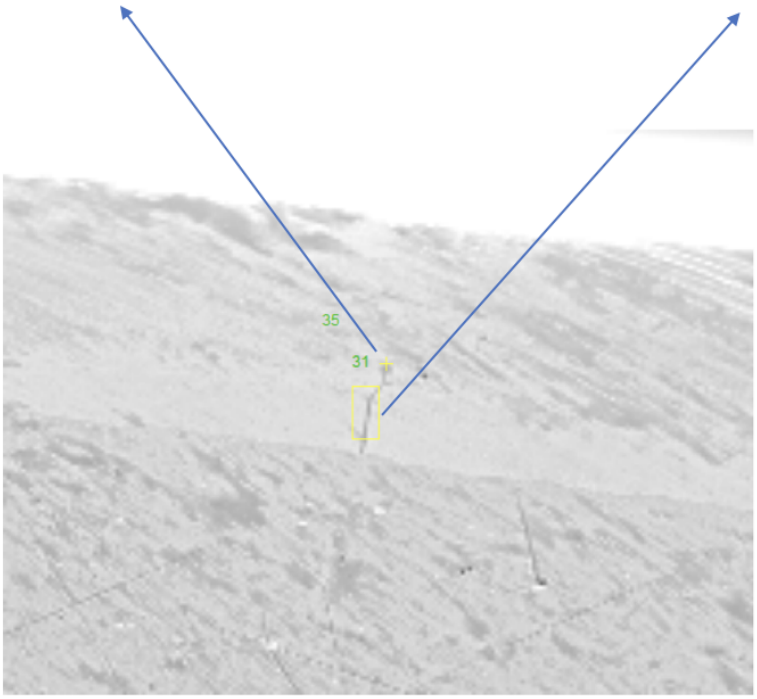

Figure 4.22: EDS measurement in a crack and a pore showing high amounts of oxygen.

Spectrum: 36

Element	norm. C [wt.%]	Atom. C [at.%]	Error (3 Sigma) [wt.%]
Aluminium	70,03	68,76	6,75
Silicon	19,98	18,85	1,79
Chromium	3,63	1,85	0,30
Oxygen	6,37	10,54	1,79
Total:	100,00	100,00	

Spectrum: 39

Element	norm. C [wt.%]	Atom. C [at.%]	Error (3 Sigma) [wt.%]
Aluminium	62,61	61,86	5,17
Silicon	21,07	20,00	1,61
Chromium	7,84	4,02	0,48
Oxygen	8,48	14,13	1,87
Total:	100,00	100,00	

Spectrum: 35

Element	norm. C [wt.%]	Atom. C [at.%]	Error (3 Sigma) [wt.%]
Chromium	10,83	5,95	0,62
Aluminium	79,30	84,00	6,24
Silicon	9,88	10,05	0,77
Total:	100,00	100,00	

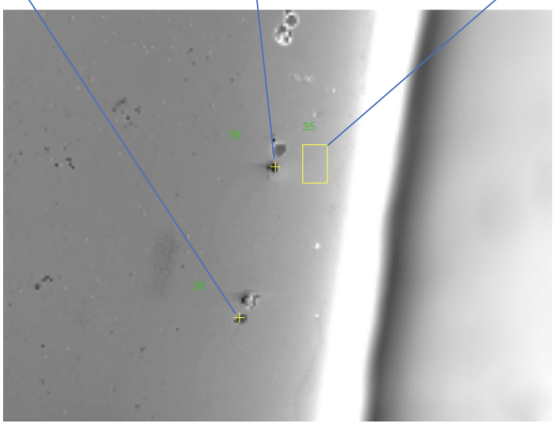

Figure 4.23: EDS measurement in two pores and one defect free area in the remelted zone. The measurements show a high amount of oxygen in the pores.

4.2 Laser surface remelting of wedge cast Al-Si-Cu alloys

Figure 4.24 shows OM pictures taken of as-cast anodised samples of the wedge cast, for alloy A and alloy B. For alloy B the grain size seems to be smallest in the middle sample and quite similar in the thick and tip samples. For alloy A the grain size is more uniform between the three samples. The SDAS for both alloys is smallest in the tip sample and largest in the sample from the thick part. It can be seen that the SDAS for alloy B is significantly finer in alloy B than in alloy A in the tip sample.

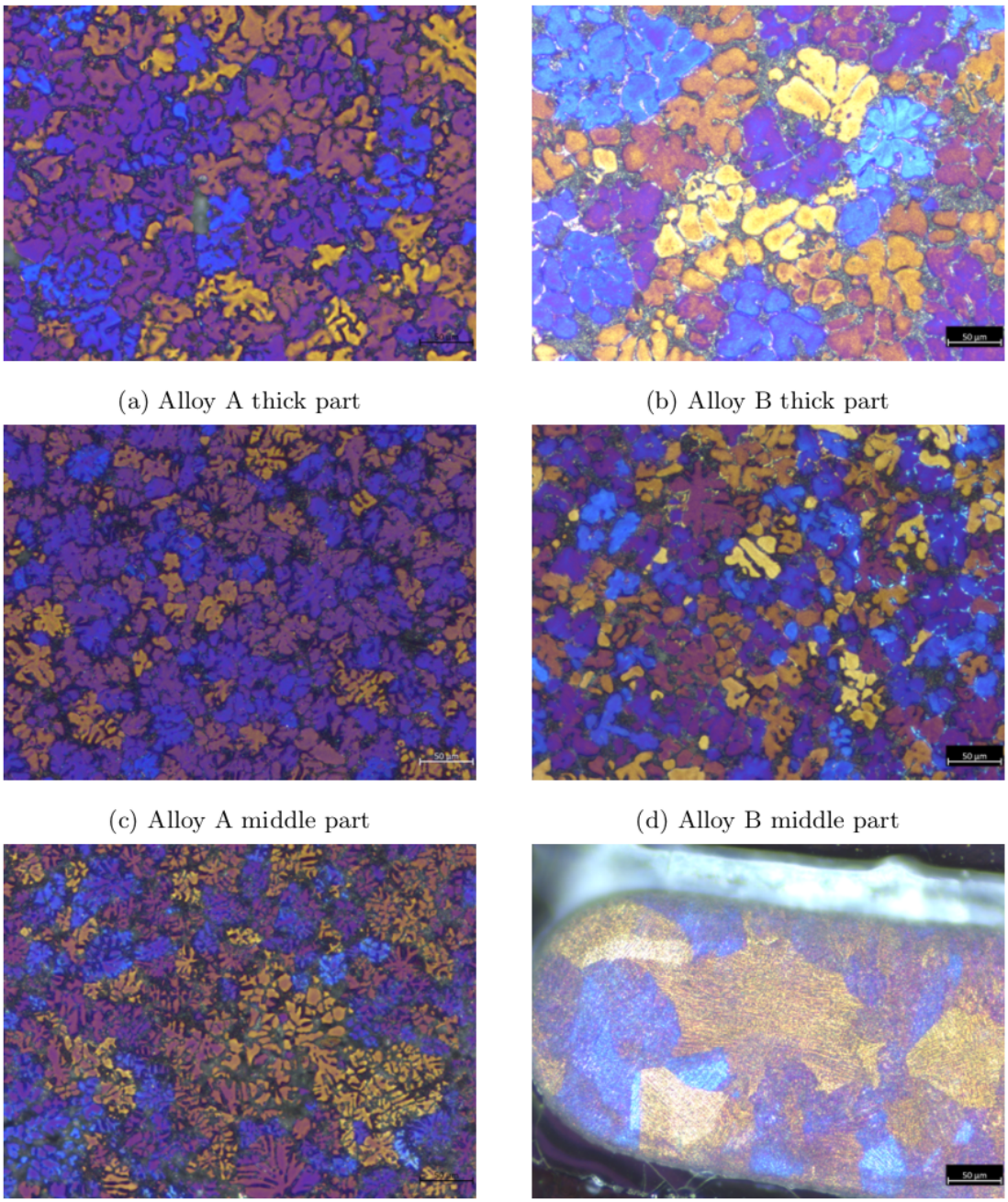

(a) Alloy A thick part

(b) Alloy B thick part

(c) Alloy A middle part

(d) Alloy B middle part

(e) Alloy A tip part

(f) Alloy B tip part

Figure 4.24: Optical microscope pictures of as-cast structure of the wedge after anodising. All scale bars have a length of 50 µm

Figure 4.25 shows the cross-section of remelted surface area on cast alloy A. The area shown is scanned with parameters 170 µm hatch distance, 370 W laser power and 1335 mm/s scanning speed with parallel lines scan strategy, a) in figure 2.2. The neighbouring lines that together create the area can clearly be distinguished from each other. The secondary dendrite arm spacing (SDAS) is much finer in the remelted zone compared to the bulk of the sample.

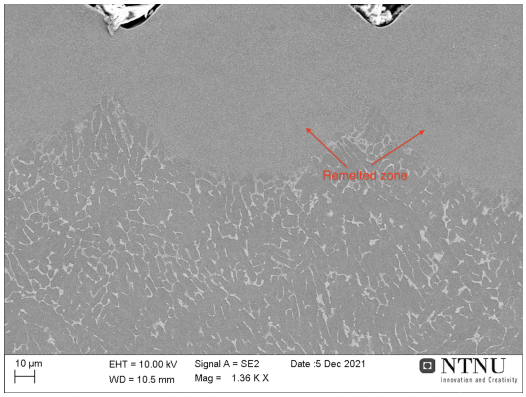

(a) Overview of the cross section of the remelted area

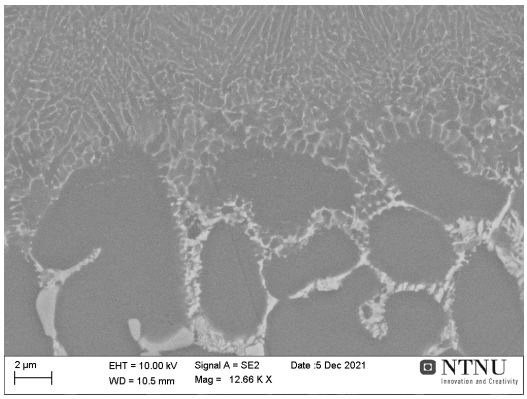

(b) Border between the remelted zone and bulk material

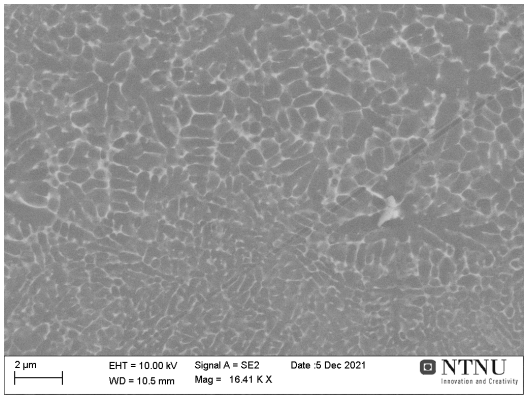

(c) Inside the remelted zone

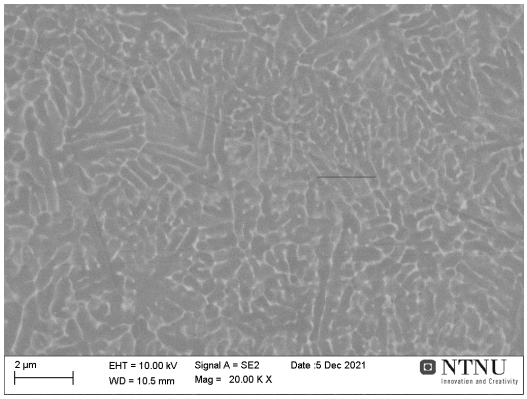

(d) Inside the remelted zone

Figure 4.25: SEM image of cross section of laser surface remelted area on cast alloy A

In figure 4.26 two remelted lines from laser scanning on alloy A can be seen. As expected the remelted zones have a much finer SDAS compared to the bulk of the sample and the transition from the coarse to the fine dendritic structure is clearly visible. The pictures to the left in the figure are of line scanned with L1 parameters, which are 1000 mm/s scanning speed and 400 W laser power. The pictures to the right are of line scanned with L2 parameters, which are 750 mm/s scanning speed and 400 W laser power. L2 has a slightly deeper remelted zone than L1, due to the slower scanning speed that leads to higher line energy.

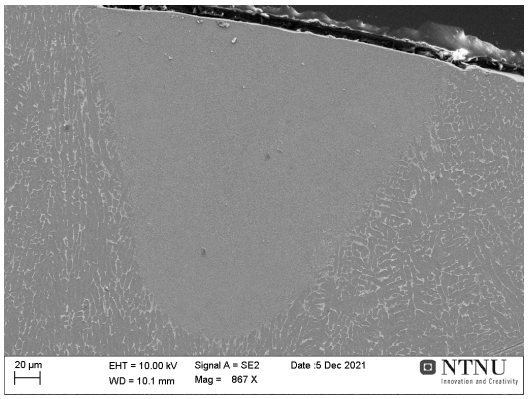

(a) Overview of L1

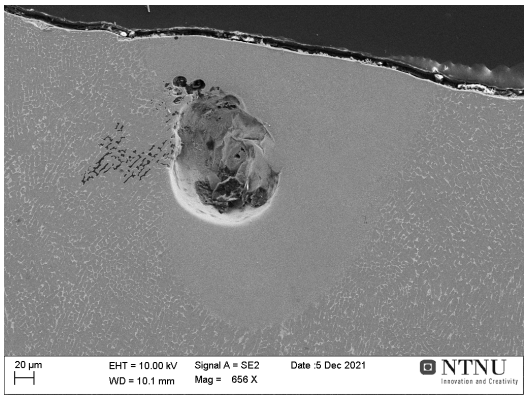

(b) Overview of L2

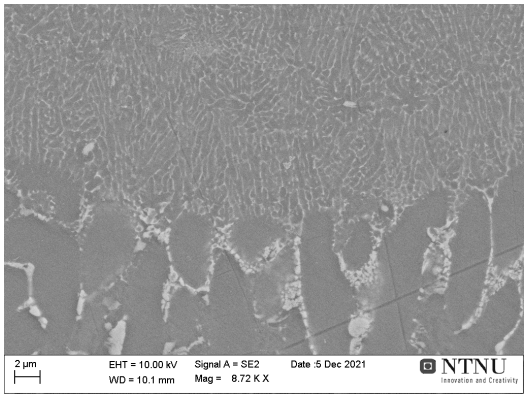

(c) Border between L1 and bulk material

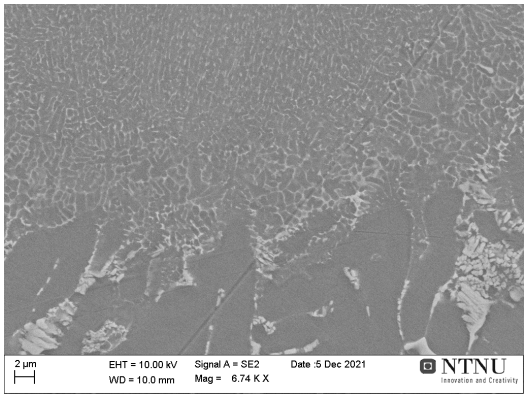

(d) Border between L2 and bulk material

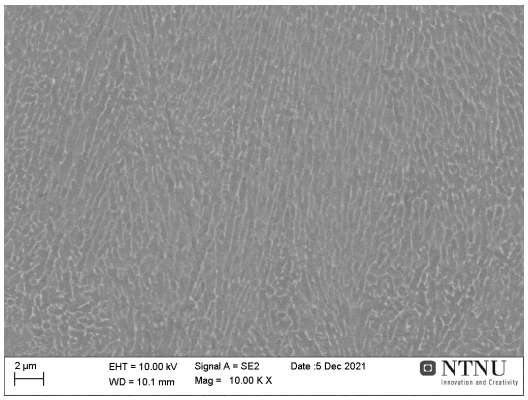

(e) Inside L1

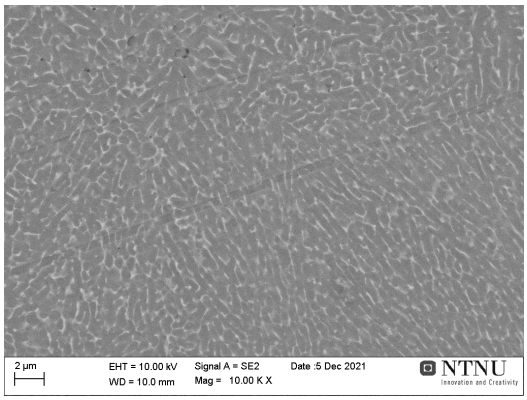

(f) Inside L2

Figure 4.26: SEM images of cross section of laser surface remelted lines on alloy A with different laser scanning parameters. L1 to the left and L2 to the right. L1: 1000 mm/s, 400W. L2: 750 mm/s, 400W.

The laser remelted surface area on alloy B is displayed in figure 4.27. The laser parameters for this area is identical to the ones for the area showed in figure 4.25, which are 170 µm hatch distance, 370 W laser power and 1335 mm/s scanning speed with parallel lines scan strategy. A dendritic structure can be seen, with much finer SDAS in the remelted zone than in the bulk of the sample. This makes it easy to distinguish between the remelted zone and the bulk.

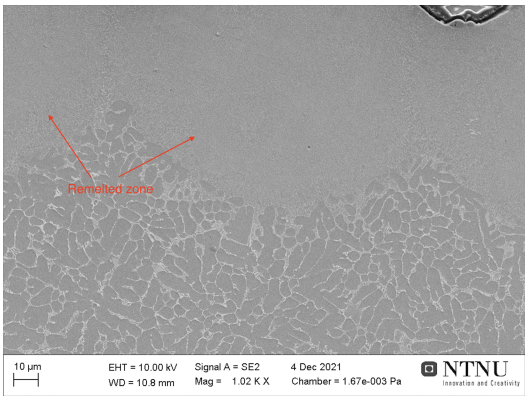

(a) Overview of the cross section of the remelted area

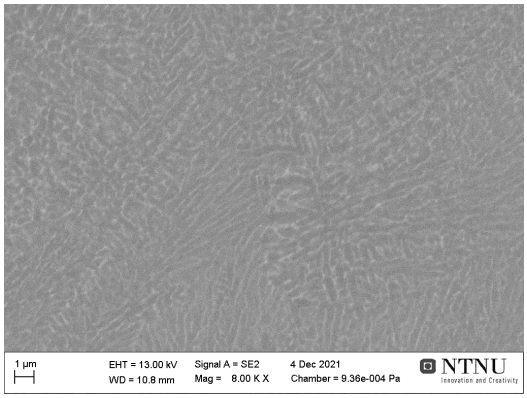

(b) Border between the remelted zone and bulk material

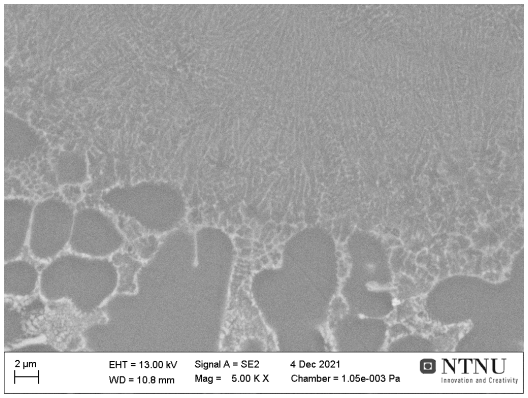

(c) Inside the remelted zone

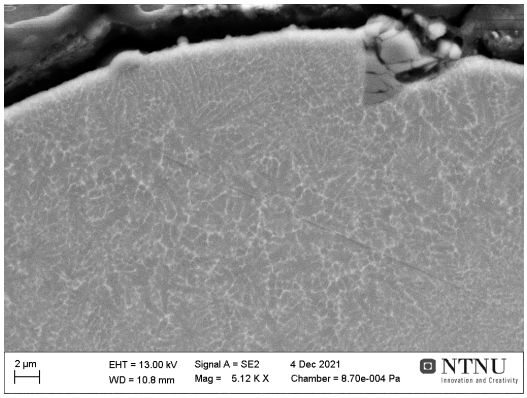

(d) Inside the remelted zone

Figure 4.27: SEM images of cross section of laser surface remelted area on cast alloy B.

In figure 4.28 two remelted lines from laser scanning on alloy B can be seen. As for the images above the SDAS is significantly finer in the remelted zone. The pictures to the left in the figure are of line scanned with L1 parameters, which are 1000 mm/s scanning speed and 400 W laser power. The pictures to the right are of line scanned with L2 parameters, which are 750 mm/s scanning speed and 400 W laser power. L2 has a slightly deeper remelted zone than L1, due to the higher line energy caused by a slower scanning speed.

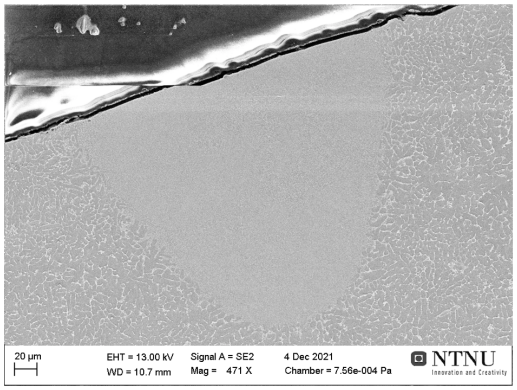

(a) Overview of L1

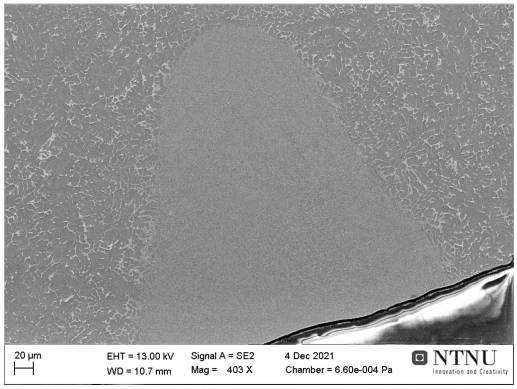

(b) Overview of L2

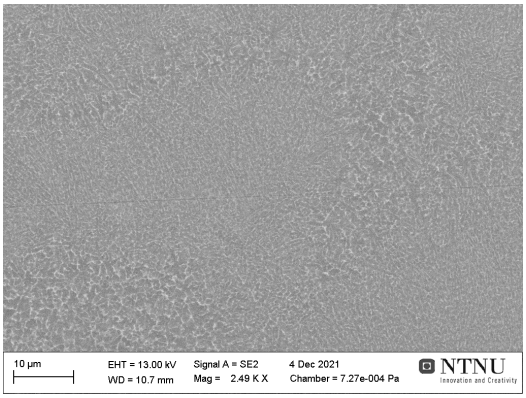

(c) Inside L1

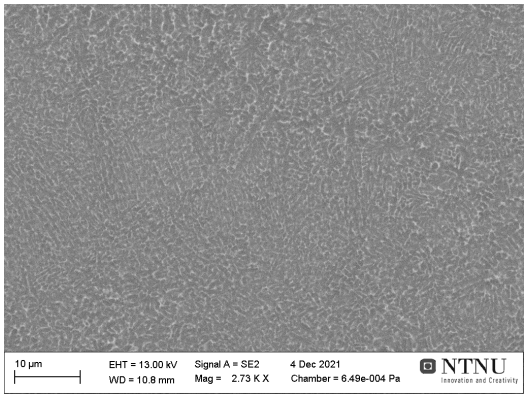

(d) Inside L2

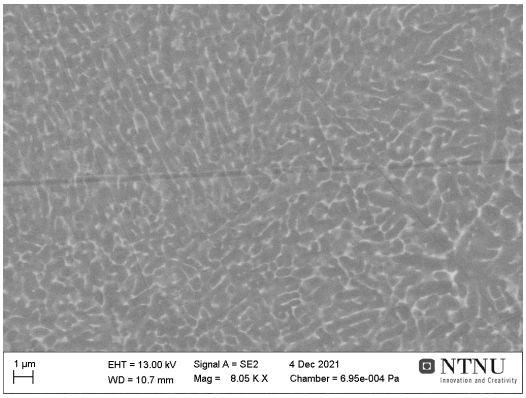

(e) Inside L1

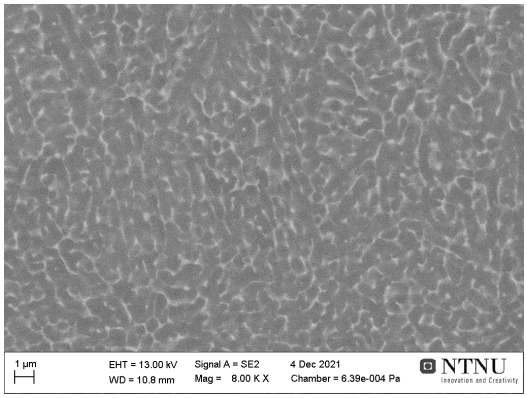

(f) Inside L2

Figure 4.28: Laser surface remelted lines on alloy B. L1 to the left and L2 to the right. L1: 1000 mm/s, 400W. L2: 750 mm/s, 400W.

As mentioned above, it can be seen from figure 4.25, 4.26, 4.27 and 4.28 that the SDAS is significantly smaller in the remelted zones compared to the bulk material. The average SDAS was measured to be 0.42 µm and 5.5 µm in the remelted zone and bulk material, respectively.

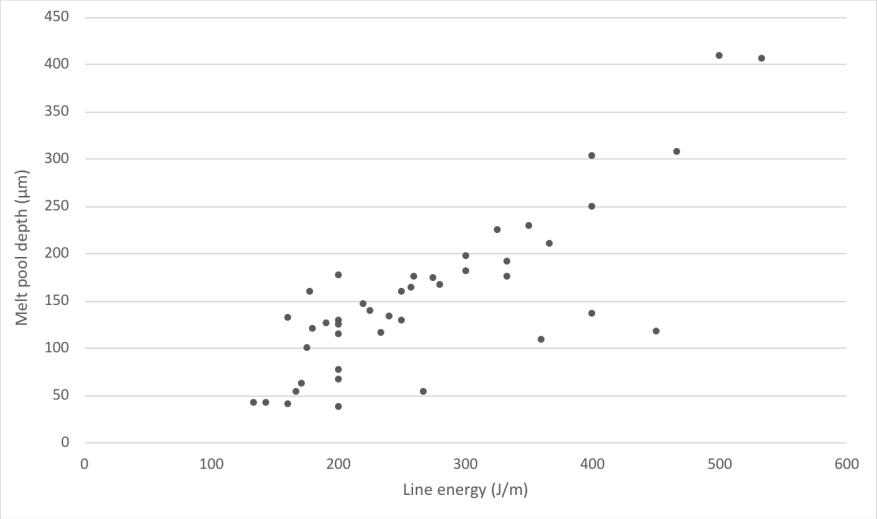

Figure 4.29: Line energy plotted against melt pool depths for scanned lines on wedge cast alloy A.

Figure 4.30 shows the EBSD map from the cross-section of the scanned area on alloy A. The grains can be distinguished from one another and the grains in the remelted zone have an equiaxed shape. It can be seen that the grains in the remelted zone are significantly smaller, compared to the grains in the bulk material. The grain refinement can also be seen by compering the grain size of the as-cast structure in figure 4.24 with the grain size in the remelted zone. The grain structure of the remelted zone of the scanned area on alloy B, which can be seen in the EBSD map in figure 4.31, is also mostly equiaxed. However, some columnar grains are present in the bottom part of the remelted zone. The grains also appear to be finer in the outer part of the remelted zone. In figure 4.31 the grains in the right part of the remelted structure appear to be finer than the grains to the left in the remelted structure. The laser parameters for the remelted cross sections in figure 4.30 and 4.31 are 170 µm hatch distance, 370 W laser power and 1335 mm/s scanning speed with parallel lines scan strategy.

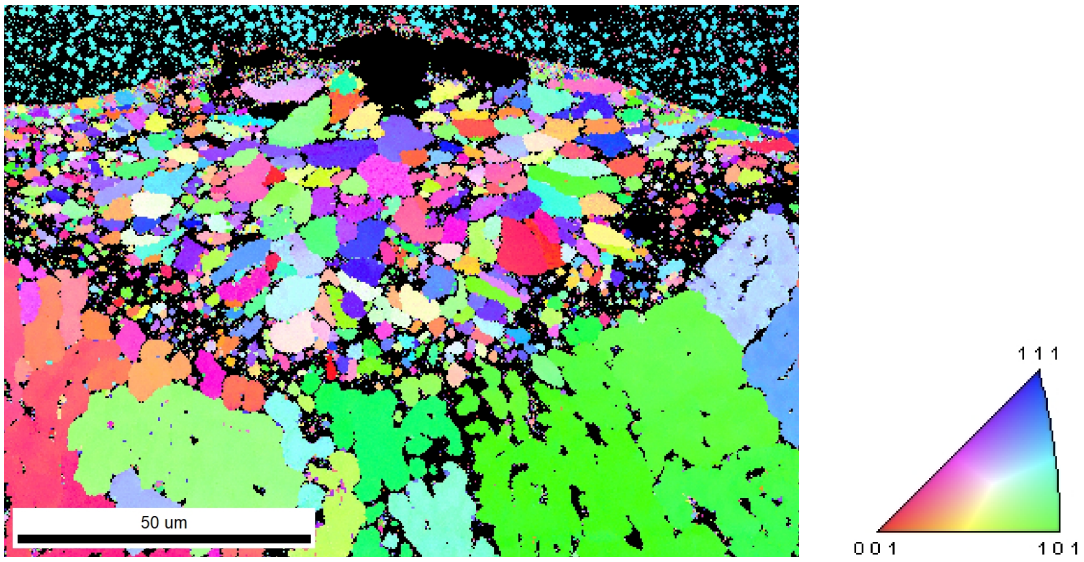

Figure 4.30: EBSD map of the cross-section of laser surface remelted area on alloy A

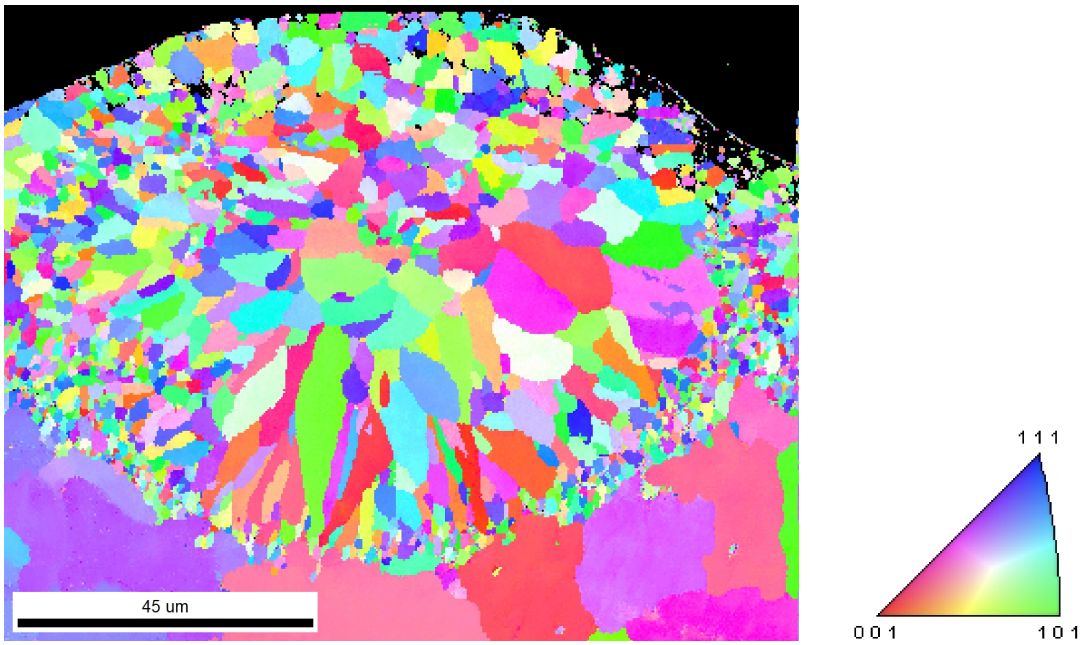

Figure 4.31: EBSD map of the cross-section of laser surface remelted area on alloy B

The EBSD map of a remelted line on alloy B is shown in figure 4.32, scanned with 400 W laser power and 1000 mm/s scanning speed. Same as the remelted areas shown above, the structure in the remelted line also has a significantly finer grain structure compared to the bulk material. The grains in the remelted zone have a more uniform size, compared to the remelted zones in figure 4.30 and figure 4.31.

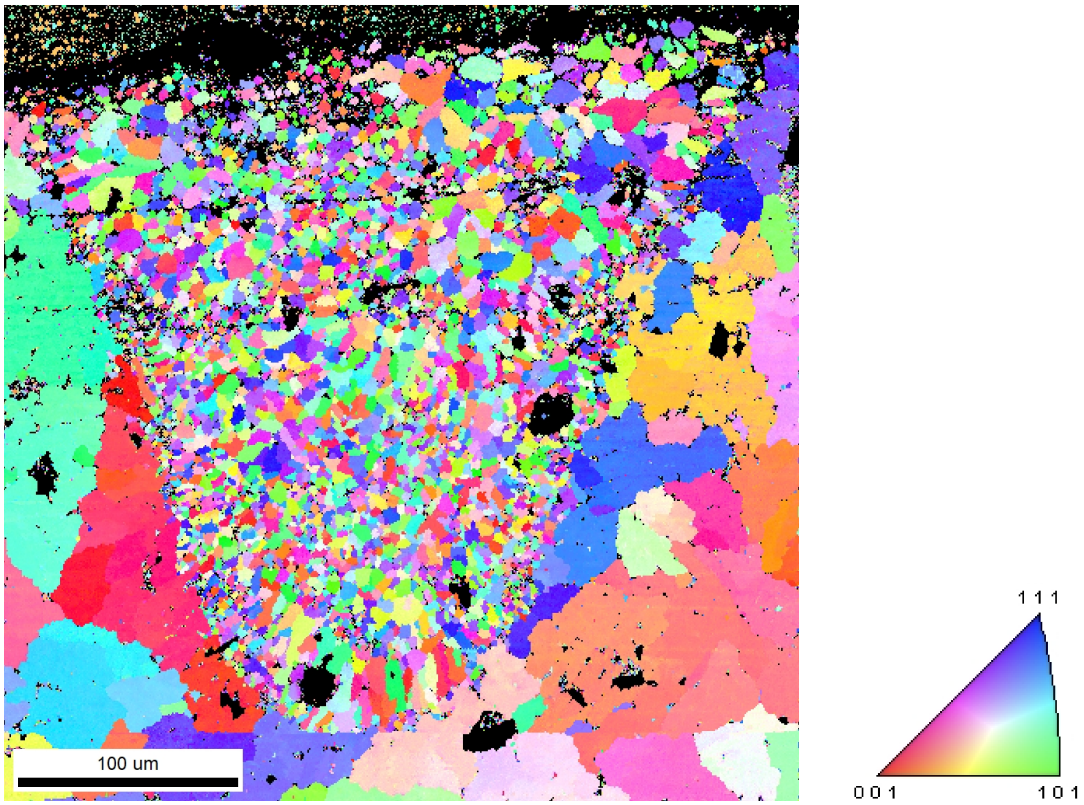

Figure 4.32: EBSD map of the cross-section of a remelted line (400W, 1000 mm/s) on alloy B

The OIM Analysis software was used to calculate the average grain size of the EBSD images. For the grain size calculations, the bulk material was cropped out, so that only the grain size in the remelted zone was calculated. The remelted zone on alloy A (figure 4.30) had an average grain diameter of 3.73 µm, for alloy B the average grain diameter in the zone (figure 4.31) was 4.83 µm. While the remelted line on alloy B had an average grain diameter of 1.9 µm. In the as cast state the tip of the wedge had an average grain diameter of 41 µm and 51 µm for alloy A and B, respectively.

The remelted zone of both alloys was harder than their bulk material. The remelted zone of alloy A had a hardness of 198.6 $HV_{0.1}$, while the bulk material had a hardness of 145.5 $HV_{0.1}$. Similar hardness was measured on alloy B where the hardness was measured to be 201.5 $HV_{0.1}$ and 152.1 $HV_{0.1}$ in the remelted zone and bulk material, respectively.

5 Discussion

5.1 AlSiCr alloys

5.1.1 Influence of alloy concentration on melt pool depths

From figure 4.5 it is evident that the same laser parameters led to different melt pool depths in the four groups. The deepest melt pools were consistently observed in group 3 for all laser parameters. The EDS measurements revealed that the film in group 3 had 8.9 wt% silicon, which made group 3 the group with silicon concentration closest to the eutectic composition. A eutectic composition is the composition with the lowest melting point within a binary eutectic alloy system. It is therefore not surprising that the deepest melt pools were found in group 3. The reflectivity of the surface, i.e. how much of the laser energy is reflected away from the surface, also affects the penetration depths of the melt pools. However, the reflectivity of the deposited surface film is expected to be reasonably uniform. The depth of the remelted zone can also be influenced by the presence of phases with a different melting temperature or reflectivity. Since single ions or clusters of ions are released from the targets during the deposition process, different phases are unlikely to be formed. Still, this could explain the inconsistent melt pool depths found for similar line energies on the remelting of the cast wedge tip. In figure 4.29 the melt pool depth and line energy follows a fairly linear relationship, with a few exceptions. The exceptions may be ascribed to phases with a different melting point being present on the cast surface. Also, since the sample was not completely flat the laser did not focus evenly on the sample surface, which would affect melt pool depths as well.

From table 5 it can be seen that penetration of the film causes the substrate metal to be mixed with the film. Since the substrate consists of very pure aluminium, it effectively dilutes the melt pool composition. In this work, penetration of the film was not desired, as it would dilute the alloys intended for characterization. In some special case, film penetration can be done intentionally to dilute the film alloys, as suggested by [47]. This would require the penetration depth of the selected laser parameter(s) to be greater than the film thickness. In this situation, a substrate alloy with various levels of alloy additions could be effectively reviewed. Film penetration could also be used to enrich the substrate alloy with the alloying elements of the film. In both the mentioned scenarios, a relatively thin film may be sufficient to reach the wanted alloy composition. Which means that a shorter deposition time is required, resulting in a cheaper and more effective alloy developing process.

5.1.2 Surface finish after laser remelting

As can be seen in figure 4.6 there was a significant difference in surface finish across the plate. From shiny and nearly mirror-like on the right side to matt and black on the left side. By also studying the simulation of silicon content distribution of the deposited film in figure 3.3, it can be seen that the matt and black surface appeared on the high silicon side of the plate. The transition from a shiny to a matt surface correlates well with the melt pool monitoring image generated by the SLM Solutions software during laser scanning, see figure 5.1. The melt pool monitoring does not directly measure the temperature of the melt pool, instead, it measures emitted heat radiation. Nevertheless, this indicates that the melt pool temperature affects the surface finish. Since the matt and black surface only are observed at the side of the plate where the film is high in silicon, the chemical composition is also likely to be a factor that affects the surface finish. The thermal conductivity of aluminium alloys will decrease with increasing silicon content [48] [49]. The parts of the film with high silicon will therefore retain more of the heat from the laser, compared to parts low in silicon. This can have led to the high silicon part of the film becoming too hot, resulting in a poor surface finish, indicating that a line energy of 200 J/m, which was used here, is too large for aluminium alloys with high amounts of silicon. This is supported by Ullsperger et al. [50] who performed selective laser remelting of an aluminium alloy with 40 wt% silicon. In their parameter study, they found that a line energy of 210 J/m resulted in high amounts of melt pool spatter and a line with poor geometrical accuracy. Although Ullsperger et al. used a low power pulsed laser, in contrast to the high power continuous wave laser used in this work, their findings back up the hypothesis that the line energy 200 J/m was too high for the high silicon parts of the plate. Their results indicate that a line energy between 100 and 150 J/m would be more appropriate for high silicon aluminium alloys.

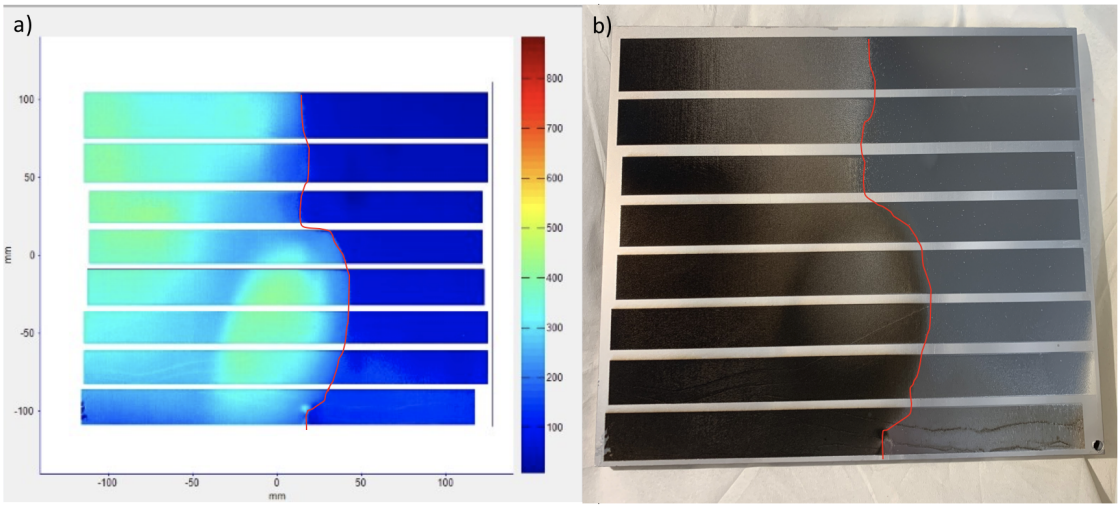

Figure 5.1: a) Melt pool monitoring from SLM solutions software. b) remelted sample. Red line showing border between shiny and matt surface.

5.1.3 Electrical conductivity

The electrical conductivity heat map in figure 4.9 display results opposite to what is expected. The top right corner, where the concentration of alloying elements is the lowest, also had the lowest electrical conductivity, see figure 3.3 for simulations of the surface film concentration. Pure aluminium is a great conductor of electricity, however, the addition of alloying elements drastically worsens its conductivity [51]. The reason for the unexpected measurements could be that the measurement depth exceeded the thickness of til film and that the underlying plate, therefore, affected the measurements. Figure 5.2 shows that the thickness of the film correlates well with the measured electrical conductivity. Where the film is thickest, the electrical conductivity is the lowest.

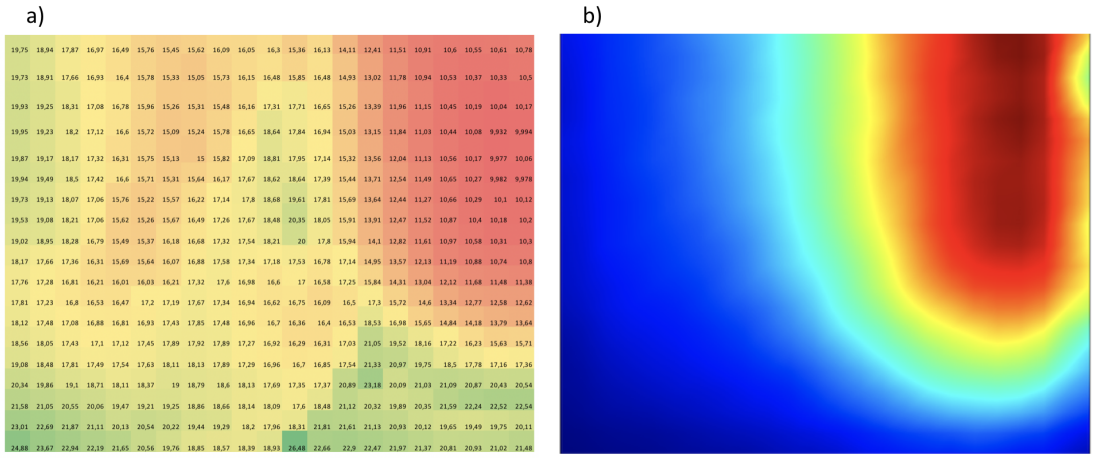

Figure 5.2: a) electrical conductivity, b) film thickness simulation.

The following equation, which describes the relationship between measurement depth and conductivity, is found in the operating manual of the Sigmatest 2.069 [52].

$$eff = \frac{503}{\sqrt{\sigma \cdot f}} \tag{17}$$

Where eff is effective penetration depth, σ is electrical conductivity and f is frequency. Figure 5.3 shows effective penetration depth on different spots on the surface, calculated by equation 17. By comparing the effective penetration depths from figure 5.3 with the film thickness simulation in figure 5.2b it can be seen that the only place where the film thickness is greater than the effective penetration depth is in the top right corner. According to the film thickness simulation seen in figure 5.2b, the red and yellow areas have a film thickness above 140 µm, the green area has a film thickness of approximately 100 µm, and the blue areas have a film thickness below 70 µm. Based on this it is likely that the yellow and red areas were the only areas on the plate where the effective penetration depth was smaller than the film thickness. However, the Sigmatest operating

manual states that an accurate measurement can not be guaranteed if the material being measured is thinner than three times the effective penetration depth. Such a film thickness exists nowhere on the plate and therefore some uncertainty is associated with all the measured electrical conductivity values. But, the highly conductive substrate plate will affect the measurements more where the film is thin. This is why the highest conductivity is measured along the bottom and left side (where the film is thin), even though this is where the concentration of alloying elements in the film is the highest.

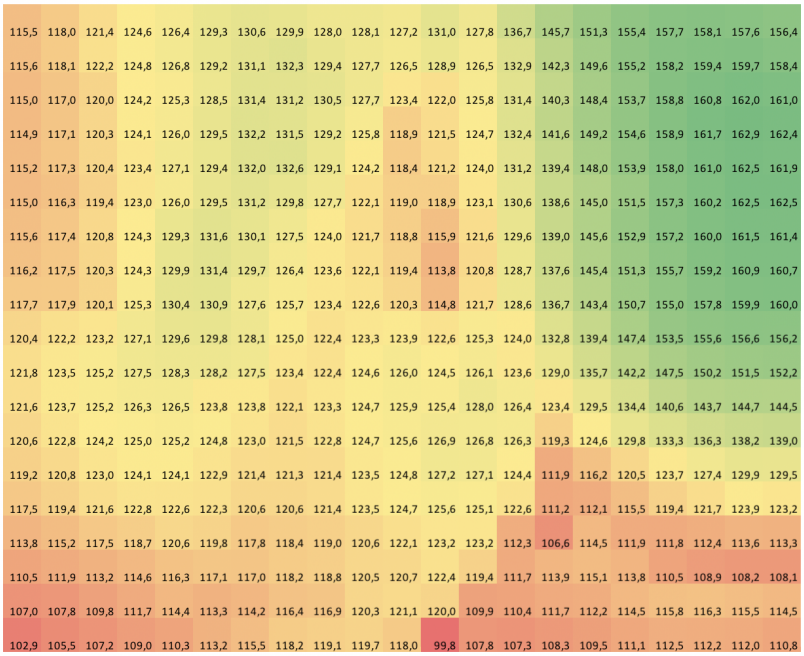

Figure 5.3: Effective penetration depth in µm, calculated with equation 17.

Even though the highest available frequency on the instrument was used, the effective penetration depth is still too large to give accurate measurements of the film's electrical conductivity. The inaccuracy of the measurements could be fixed by depositing a thicker film or using an instrument with a shallower penetration depth. On the other side, if the substrate metal and the film have a big difference in conductivity, the Sigmatest could be used to detect variations in film thickness. Which could be helpful to confirm the thickness distribution predicted by a simulation or if no simulation is available. However, it is important to note that this alternative use of an electrical conductivity measurement instrument only may provide information about variation in film thickness and limited information about the actual film thickness.

5.1.4 Hardness measurements

The rough surface of the matt and black area makes hardness measurements difficult in these areas. The accuracy of the hardness measurements in these areas is therefore highly questionable. The

hardness values in these areas do not vary as evenly as in the shiny areas, and they seem more random than what is expected from a gradual change in chemical composition. A larger load would increase the accuracy of the measurements, especially in the areas with a rough surface. But, a relatively small load of 500 grams was chosen to avoid the indenter penetrating through the film and into the substrate. Vickers hardness test works best on a flat surface; the precision of the hardness measurements could therefore also be improved by polishing the surface. However, this was not done to avoid polishing away the thin surface layer. The thinnest part of the film exists in the places where polishing would be necessary, polishing away the whole film was, therefore, a real possibility. That issue could, of course, be resolved by depositing a thicker film. However, a thicker film would require a longer deposition time, which would drive up the price of the alloy development. On the other side a thicker film would make it possible to use a larger load for indenting or perform some polishing with out the risk of penetrating the film, both would increase the accuracy of the measurements. Both a larger load and polishing can make more clear indentations, making it easier for the software to detect them, making the process more automatic. The fact that each of the over 500 indentations had to be measured manually meant that the hardness measurements took a very long time. Therefore, the longer deposition time required to create a thicker film could be compensated for by saving time on a more automated hardness measuring process.

5.1.5 Influence of alloy concentration on crack and porosity formation

The observed cracks in the cross-section of the remelted zone of the single line scans, from the top part of the AlSiCr plate were all for the lines with higher line energy. As stated in the theory (chapter 2), solidification cracking is a defect that can occur if an alloy experiences high levels of stress during solidification. Due to the melt pool penetrating through the film and into the substrate below the film concentration was diluted. Resulting in a melt pool concentration very low in silicon, roughly 2-3 wt% silicon, see table 5. The aluminium silicon phase diagram, in figure 2.6, shows that such an alloy will have a large solidification range, which increases the susceptibility to solidification cracking.

The porosities and cracks had a high amount of oxygen, according to the EDS measurements. As described in chapter 2.2, oxidation promotes porosities and defects like pores and cracks often have a high oxygen content. Although, both the physical vapour deposition of the surface film and the laser surface remelting were performed in an inert environment, small amounts of oxygen will almost always be present. The oxygen may therefore originate from either the deposition process, the laser surface remelting or both. The oxygen has most likely gathered via diffusion to create the high concentrations showed in figure 4.22 and 4.23.

Cracks were observed for silicon and chromium amounts between 10.6-12.5 wt% and 2.3-4.3 wt% (measured with EDS), respectively, as shown in figure 4.12. The eutectic composition in the aluminium-silicon binary phase diagram is 12.6 wt% Si, which can be seen from figure 2.6 Finding

cracks in alloys with silicon concentration in the vicinity of the eutectic composition is not expected. A eutectic alloy or alloys close to the eutectic composition have a short solidification range, producing short dendrite arms that lower the probability of melt getting entrapped and produce cracks upon solidification. Silicon also expands during solidification and therefore compensates for the shrinkage of aluminium, which further reduces the chance of cracking. Nevertheless, the findings suggest that these alloy ranges are unsuited for SLM, see figure 5.4. However, the alloy compositions may not be the cause of the crack formation. For example, oxygen levels above optimal may have been present during the deposition or the laser surface remelting process. The probability for crack formation can also be reduced by increasing the preheating temperature, due to the slower cooling rate and more gentle temperature gradient that follows.

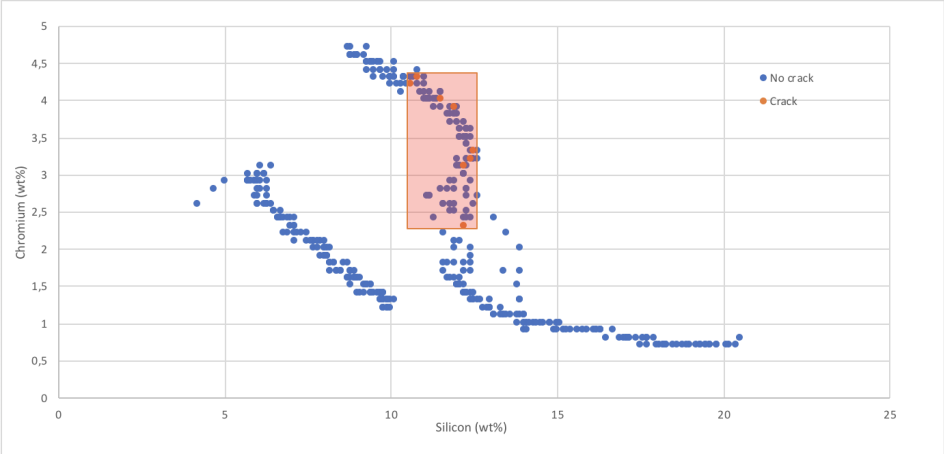

Figure 5.4: Combinations of Silicon and Chromium checked for surface cracks. Red area represents the alloy range were cracks were found.

Laser surface remelting of the deposited film have a big advantage for mapping a chemical composition range of certain alloy systems. Many alloys are subjected to conditions similar to those found in SLM and several alloys can therefore be tested simultaneously. However, each alloy composition might only exist in a small area, limiting the amount of testing possible to conduct on each alloy. This is especially true if three or more elements are deposited on to the surface. If only two elements are used a similar gradient to what is shown in the top part of the simulations in figure 3.3, can be obtained. If such a gradient is created an alloy composition may exist over a relative large distance along one axis. On the other side if more three or more elements are used, the films composition will vary across both the axis of the plane and a specific alloy may only exist in one place. This technique might also not be suitable for testing at elevated temperatures. At temperatures where diffusion can no longer be neglected, the gradient film may start to even out if kept at a high temperature for too long, effectively removing specific alloy compositions from the film.

5.1.6 Cross-section microstructure

Figure 4.14, 4.16, 4.19 and 4.21 show microstructure of selected alloys. The alloys in 4.19 and 4.21 display a fine dendritic microstructure with a small spherical pores evenly distributed in the structure. During tension the stress is concentrated in the pores, and therefore makes the alloy fail at a smaller load than in a sample with no pores. These alloys(21 wt% Si + 0.9 wt% Cr and 15.1 wt% Si + 2 wt% Cr) are therefore not suited for SLM with the process parameters used in this work. However, the porosity could likely be reduced by optimizing the process parameters, optimizing the process parameters has been proven as an effective approach to reducing pores in SLM [19][1]. The hardness of the AlSi-Si21-Cr-0.9 was measured to 254 $HV_{0.1}$, which gives an estimated yield strength of 508 MPa, if the approximation $\sigma_y = 2 \cdot HV$ is applied [53]. If a defect free microstructure of this alloy was achieved with SLM it could be very strong. The AlSi21Cr-0.9 is probably preferred over the AlSi15.1Cr2, due to the more equiaxed dendrite structure, the dendrite structures can be seen in figure 4.19 and 4.21.

The samples in figure 4.14 and 4.16 have a relatively high contents of both silicon and chromium, 12.6 wt% Si + 10.6 wt% Cr and 9.9 wt% Si + 10.6 wt% Cr, respectively. They display a similar microstructure with fine spherical particles evenly distributed in the matrix. Pores only exist in the boundary between film and remelted zone and not in the bulk of the remelted zone. The hardness was measured to 190 $HV_{0.1}$ in the AlSi12.6Cr10.6 alloy, since the microstructure and composition is similar to the AlSi9.9Cr10.6 alloy the hardness of this alloy is most likely very similar. This gives an estimated yield strength of 380 MPa, if the approximation $\sigma_y = 2 \cdot HV$ is used. The small and evenly distributed particles is likely to give the alloy strength by hindering the movement of dislocations, similar to precipitates created during precipitation hardening. Small particles leads to less stress concentration compared to larger particles, the round shape of the particles is also advantageous with regards to lowering stress concentrations.

5.2 AlSiCu alloys

It can be seen from figure 4.24 that the SDAS of the as-cast structure is finer in the tip sample of alloy B and coarser in the tip sample of alloy A. Due to a casting defect the tip sample from alloy A had to be taken in a wider position of the wedge than for alloy B, meaning that the cooling rate in the tip sample of alloy A was not as fast as in the tip sample of alloy B. Therefore resulting in a larger SDAS in alloy A, since a faster cooling rate leads to a finer SDAS, as described in chapter 2.3. This is also the reason why the SDAS is smaller in the samples close to the wedge tip, where the cooling rate is the highest.

5.2.1 Cooling rate

The secondary dendrite arm spacing (SDAS) was measured to be 0.42 µm in the remelted zone on the cast alloys and 5.5 µm in the as-cast structure at the tip of the wedge. Equation 9 and equation 10 state that the SDAS are a function of cooling rate. Since the SDAS of the remelted zone and the tip of the wedge have been measured, their relative difference in cooling rate can be calculated. The t_f factor in equation 9 are to the power $\frac{1}{3}$, therefore the difference in cooling rate will be the cube of the difference in SDAS. $\frac{5.5^3}{0.42^3} = 2246$, according to this calculation the cooling rate in the remelted zones is more than 2200 times quicker than the cooling rate of the wedge tip. As stated by Jia et al. [4] the cooling rate in the tip of the wedge copper mould can reach up to 1000 K/s, their casting conditions can have been different than in this work, this is just an estimate. If the cooling rate in the wedge tip is estimated to be 1000 K/s, it means that the cooling rate can have reached over two million Kelvin per second in the remelted zones. Which is similar to the cooling rates reported for SLM in the literature [1][4][54].

5.2.2 Grain refinement

The average grain size in the remelted area for both alloy A and B was over ten times smaller than in the bulk material, with a reduction from 41 µm to 3.73 µm for alloy A and 51 µm to 4.83 µm for alloy B, meaning that a successful grain refinement was achieved in the designed alloys. The refinement of the structure is due to the increased cooling rate and a sufficient amount of nucleation sites and consitution undercooling. Titanium and zirconium create effective heterogeneous nucleation sites for α-aluminium via the particles Al_3Ti and Al_3Zr, respectively. It is important to consider both the nucleant and solute effects of an element when dealing with grain refinement. The growth restriction factor (GRF) is used as a measurement on how powerful solute effect an element has. Titanium has a very high GRF, and it has been suggested that the main reason for titanium's grain refinement effect on aluminium alloys is the creation of a constitutional undercooled zone where nucleation can occur [55]. On the other side, zirconium has a low GRF and the grain refinement caused by zirconium is credited to nucleant effects [56]. Therefore, the grain refinement observed is likely a product of the excellent solute effects of titanium and the Al_3Ti and Al_3Zr nucleation sites. It is feasible that the grain refinement mechanisms that lead to the grain refinement in the remelted zones need a ultra high cooling rate to be effective, since not much grain refinement was seen in the tip samples of the as-cast structure, showed in figure 4.24. This area also has a relatively rapid cooling rate, however it is slow when compared to the cooling rate of the remelted zone.

The reduction of average grain diameter will increase the yield strength of the alloy, as described by the Hall-Petch relationship (equation 1). An increase in strength should also be credited to supersaturation of alloying elements, caused by the very rapid cooling rate. The columnar grain

structure of an AlSi10Mg component built with SLM is shown in figure 5.5; this structure can easily occur in SLM if not an appropriate alloy or laser parameters are used. The steep temperature gradients which are associated with the SLM process facilitate the formation of columnar grains [6] [57]. An equiaxed grain structure holds several advantages over a columnar structure, an equiaxed structure is less susceptible to solidification cracking and the mechanical properties are the same in every direction (isotropic behaviour). While, a columnar grain structure is susceptible to solidification cracking and the tensile properties are good in the longitudinal direction of the grains, but poor perpendicular to them. The formation of columnar grains therefore indicates that these alloys are well suited for the high cooling rates and temperature gradients of SLM and other PBF techniques.

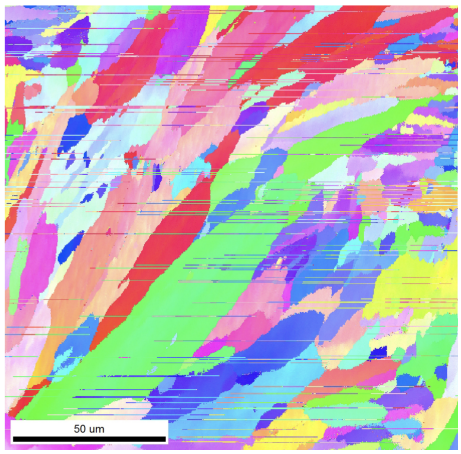

Figure 5.5: Columnar grain structure of AlSi10Mg produced with SLM [58].

The average grain diameter in the remelted line was notable smaller compared to the average grain diameter of the remelted area on the same alloy, 4.83 µand 1.9 µm for the area and the line, respectively. The remelted surface area consists of several closely scanned lines, as opposed to just a single line. During the scan of a line, its neighbouring lines will also be heated up, as a result, a remelted surface area will have a slower cooling rate than a single remelted line. The slower cooling rate has led to the remelted surface area having a more coarse grain structure than the single remelted line, as shown by figure 2.7. The grain size difference within the remelted zone shown in figure 4.31 could indicate an uneven cooling rate within the remelted zone, with a higher cooling rate in the left part of the remelted zone. The reason for this could be that the lines that make up the area were scanned from left to right, meaning that the left side of the remelted zone is adjacent to an already solidified line, which will emit less heat than the newly scanned line next to the right side of the remelted zone. However, the direction of the laser scanning relative to the remelted zone in figure 4.31 is unknown. The quality of the EBSD image in figure 4.30 is not sufficient to identify if a local grain size difference is present there as well.

6 Conclusion

- Two alloy development techniques for AM was utilized. Laser remelting of a deposited surface gradient proved to be an effective approach to characterize a large range of alloy combinations and to identify alloy regions not suited for AM.
- The Al-Si12.6-Cr10.6 and Al-Si9.9-Cr10.6 alloys looks promising for use in AM. Both alloys had no porosity in the bulk, they are outside the area where cracks were detected and their hardness values are good. The high density of fine intermetallic particles are likely to give an increase in strength.
- The two AlSiCu alloys experienced significant grain refinement during laser remelting, an equiaxed grain structure was achieved and a hardness of around 200 $HV_{0.1}$ were measured in the remelted zones. Also, the remelted zones were crack and porosity free. These results indicate that the designed AlSiCu alloys are suitable for SLM and other AM processes.

6.1 Further work

- The microstructure of the Al-Si12.6-Cr10.6 and Al-Si9.9-Cr10.6 alloys should be characterized in more detail, for example average grain size, chemical compositions and volume fraction of the fine intermetallic particles should be further investigated.
- Optimization of process parameters for the Al-Si21-Cr-0.9 with regards to porosity reduction and improvement of surface quality could, if successful, produce a very strong aluminium alloy for AM.

Bibliography

[1] H. Rao, S. Giet, K. Yang, X. Wu and C. H. Davies, *The influence of processing parameters on aluminium alloy A357 manufactured by Selective Laser Melting*, English, Materials and Design, Volume 109, 2016, Pages 334-346. https://doi.org/10.1016/j.matdes.2016.07.009.

[2] C. Y. Yap, K. Chua, Z. Dong *et al.*, 'Review of selective laser melting: Materials and applications', *Applied Physics Reviews*, vol. 2, p. 041 101, Dec. 2015. DOI: 10.1063/1.4935926.

[3] J. Martin, B. Yahata, J. Hundley and et al., *3D printing of high-strength aluminium alloys.* English, Nature 549, 365–369 (2017). https://doi.org/10.1038/nature23894.

[4] Q. Jia, P. Rometsch, S. Cao, K. Zhang and X. Wu, *Towards a high strength aluminium alloy development methodology for selective laser melting*, English, Materials and Design, Volume 174, 2019, 107775. https://doi.org/10.1016/j.matdes.2019.107775.

[5] M. Moorehead, K. Bertsch, M. Niezgoda *et al.*, 'High-throughput synthesis of Mo-Nb-Ta-W high-entropy alloys via additive manufacturing', *Materials & Design*, vol. 187, p. 108 358, 2020, ISSN: 0264-1275. DOI: 10.1016/j.matdes.2019.108358.

[6] J. Martin, B. Yahata, J. Hundley and et al., *3D printing of high-strength aluminium alloys.* English, Nature 549, 365–369 (2017). https://doi.org/10.1038/nature23894.

[7] B. Zhang, Y. Li and Q. Bai, *Defect Formation Mechanisms in Selective Laser Melting: A Review*, English, Chin. J. Mech. Eng. 30, 515–527 (2017). https://doi.org/10.1007/s10033-017-0121-5.

[8] G. P.-d. León, V. E. Lamberti, 2. D. Seals, T. M. Abu-Lebdeh and S. A. Hamoush, *Gas Atomization of Molten Metal: Part I. Numerical Modeling Conception*, English, DOI:10.3844/ajeassp.2016.303.322.

[9] J. Zhang, B. Song, Q. Wei, D. Bourell and Y. Shi, 'A review of selective laser melting of aluminum alloys: Processing, microstructure, property and developing trends', *Journal of Materials Science & Technology*, Recent Advances in Additive Manufacturing of Metals and Alloys, vol. 35, no. 2, pp. 270–284, Feb. 2019, ISSN: 1005-0302. DOI: 10.1016/j.jmst.2018.09.004.

[10] J. K. Solberg, *Material Science and engineering.* Norwegian University of Science and Technology, 2017.

[11] J. William D. Callister and D. G. Rethwisch, *Material Science and engineering.* Wiley, 2015.

[12] R. Ahmad, 'The effect of chromium addition on fluidity, microstructure and mechanical properties of aluminium lm6 cast alloy', *International Journal of Material Science and Research*, vol. 1, pp. 32–35, Jun. 2018. DOI: 10.18689/ijmsr-1000105.

[13] K. Kashyap and T. Chandrashekar, *Effects and mechanisms of grain refinement in aluminium alloys*, English, Bull Mater Sci 24, 345–353 (2001). https://doi.org/10.1007/BF02708630.

[14] P. Schumacher, A. L. Greer, J. Worth *et al.*, *New studies of nucleation mechanisms in aluminium alloys: implications for grain refinement practice*, English, BMaterials Science and Technology, 14:5, 394-404 (1998). DOI: 10.1179/mst.1998.14.5.394.

[15] O. S. I. Fayomi, A. P. I. Popoola and N. E. Udoye, *Effect of Alloying Element on the Integrity and Functionality of Aluminium-Based Alloy*, English, 2017. DOI: 10.5772/intechopen.71399.

[16] J. Robson and P. Prangnell, *Dispersoid precipitation and process modelling in zirconium containing commercial aluminium alloys*, English, Acta Materialia, Volume 49, Issue 4, 2001, Pages 599-613, ISSN 1359-6454. https://doi.org/10.1016/S1359-6454(00)00351-7.

[17] F. WANG, D. QIU, Z.-l. LIU, J. TAYLOR, M. EASTON and M.-x. ZHANG, 'Crystallographic study of Al3Zr and Al3Nb as grain refiners for Al alloys', *Transactions of Nonferrous Metals Society of China*, vol. 24, no. 7, pp. 2034–2040, 2014, ISSN: 1003-6326. DOI: 10.1016/S1003-6326(14)63309-4.

[18] L.-C. Zhang, Y. Liu, S. Li and Y. Hao, 'Additive Manufacturing of Titanium Alloys by Electron Beam Melting: A Review', *Advanced Engineering Materials*, vol. 20, no. 5, p. 1 700 842, 2018, ISSN: 1527-2648. DOI: 10.1002/adem.201700842.

[19] N. T. Aboulkhair, N. M. Everitt, I. Ashcroft and C. Tuck. 'Reducing porosity in AlSi10Mg parts processed by selective laser melting'. English. Additive Manufacturing, Volumes 1–4, 2014, Pages 77-86 https://doi.org/10.1016/j.addma.2014.08.001. ().

[20] L. Jiao, Z. Chua, S. Moon, J. Song, G. Bi and H. Zheng, *Femtosecond Laser Produced Hydrophobic Hierarchical Structures on Additive Manufacturing Parts*, English, Nanomaterials 2018, 8, 601 https://doi.org/10.3390/nano8080601.

[21] D. Ding, Z. Pan, D. Cuiuri and H. Li, 'Wire-feed additive manufacturing of metal components: Technologies, developments and future interests', *International Journal of Advanced Manufacturing Technology*, vol. 81, May 2015. DOI: 10.1007/s00170-015-7077-3.

[22] G. Langelandsvik, O. Ragnvaldsen, F. J.E., O. Akselsen and H. Roven, *Wire and Arc Additive Manufacturing with TiC-Nanoparticle Reinforced AA5183 Alloy*, English, https://doi.org/10.1051/matecconf/202032607002.

[23] C. Galy, E. Le Guen, E. Lacoste and C. Arvieu, 'Main defects observed in aluminum alloy parts produced by SLM: From causes to consequences', *Additive Manufacturing*, vol. 22, pp. 165–175, Aug. 2018, ISSN: 2214-8604. DOI: 10.1016/j.addma.2018.05.005.

[24] T. Ullsperger, G. Matthäus, L. Kaden *et al.*, *Selective laser melting of AlSi40 using ultrashort laser pulses for additive manufacturing applications*, 2017.

[25] G. Langelandsvik, T. Furu, H. J. Roven and O. M. Akselsen, '(PDF) Review of Aluminum Alloy Development for Wire Arc Additive Manufacturing', *ResearchGate*, 2021. DOI: 10.3390/ma14185370.

[26] T. Kimura and T. Nakamoto, 'Microstructures and mechanical properties of A356 (AlSi7Mg0.3) aluminum alloy fabricated by selective laser melting', *Materials and Design*, vol. 89, pp. 1294–1301, Jan. 2016, ISSN: 0264-1275. DOI: 10.1016/j.matdes.2015.10.065.

[27] C. Weingarten, D. Buchbinder, N. Pirch, W. Meiners, K. Wissenbach and R. Poprawe, 'Formation and reduction of hydrogen porosity during selective laser melting of AlSi10Mg', *Journal of Materials Processing Technology*, vol. 221, pp. 112–120, Jul. 2015, ISSN: 0924-0136. DOI: 10.1016/j.jmatprotec.2015.02.013.

[28] R. Rashid, S. H. Masood, D. Ruan, S. Palanisamy, R. A. Rahman Rashid and M. Brandt, 'Effect of scan strategy on density and metallurgical properties of 17-4PH parts printed by Selective Laser Melting (SLM)', *Journal of Materials Processing Technology*, vol. 249, pp. 502–511, Nov. 2017, ISSN: 0924-0136. DOI: 10.1016/j.jmatprotec.2017.06.023.

[29] H. Jia, H. Sun, H. Wang, Y. Wu and H. Wang, 'Scanning strategy in selective laser melting (SLM): A review', *The International Journal of Advanced Manufacturing Technology*, vol. 113, no. 9, pp. 2413–2435, Apr. 2021, ISSN: 1433-3015. DOI: 10.1007/s00170-021-06810-3.

[30] M. Tang and P. C. Pistorius, 'Oxides, porosity and fatigue performance of AlSi10Mg parts produced by selective laser melting', *International Journal of Fatigue*, Fatigue and Fracture Behavior of Additive Manufactured Parts, vol. 94, pp. 192–201, Jan. 2017, ISSN: 0142-1123. DOI: 10.1016/j.ijfatigue.2016.06.002.

[31] E. Olakanmi, R. Cochrane and K. Dalgarno, *A review on selective laser sintering/melting (SLS/SLM) of aluminium alloy powders: Processing, microstructure, and properties*, English, Progress in Materials Science, Volume 74, 2015, Pages 401-477. https://doi.org/10.1016/j.pmatsci.2015.03.002.

[32] S. Liu and H. Guo, 'Balling Behavior of Selective Laser Melting (SLM) Magnesium Alloy', *Materials*, vol. 13, no. 16, p. 3632, Aug. 2020, ISSN: 1996-1944. DOI: 10.3390/ma13163632.

[33] R. Li, J. Liu, Y. Shi and et al., *Balling behavior of stainless steel and nickel powder during selective laser melting process.* English, Int J Adv Manuf Technol 59, 1025–1035 (2012). https://doi.org/10.1007/s00170-011-3566-1.

[34] D. W. Kurz and P. D. J. Fisher, *Fundamentals of Solidification.* Trans Tech Publications, 1998.

[35] T. Kannengiesser and T. Boellinghaus, *Hot cracking tests—an overview of present technologies and applications*, English, Weld World 58, 397–421 (2014). https://doi.org/10.1007/s40194-014-0126-y.

[36] R.-p. LIU, Z.-j. DONG and Y.-m. PAN, *Solidification crack susceptibility of aluminum alloy weld metals*, English, Transactions of Nonferrous Metals Society of China, Volume 16, Issue 1, 2006, Pages 110-116. https://doi.org/10.1016/S1003-6326(06)60019-8.

[37] N. T. Aboulkhair, I. Maskery, C. Tuck, I. Ashcroft and N. M. Everitt, 'The microstructure and mechanical properties of selectively laser melted AlSi10Mg: The effect of a conventional T6-like heat treatment', *Materials Science and Engineering: A*, vol. 667, pp. 139–146, Jun. 2016, ISSN: 0921-5093. DOI: 10.1016/j.msea.2016.04.092.

[38] N. Read, W. Wang, K. Essa and M. M. Attallah, 'Selective laser melting of AlSi10Mg alloy: Process optimisation and mechanical properties development', *Materials & Design (1980-2015)*, vol. 65, pp. 417–424, Jan. 2015, ISSN: 0261-3069. DOI: 10.1016/j.matdes.2014.09.044.

[39] D. J. Muelaner, *The Importance of Surface Finish in Additive Manufacturing*, English.

[40] E. Maleki, S. Bagherifard, M. Bandini and M. Guagliano, *Surface post-treatments for metal additive manufacturing: Progress, challenges, and opportunities*, English, Additive Manufacturing, Volume 37, 2021, 101619, ISSN 2214-8604. https://doi.org/10.1016/j.addma.2020.101619.

[41] E. Uhlmann, C. Fleck, G. Gerlitzky and F. Faltin, 'Dynamical Fatigue Behavior of Additive Manufactured Products For a Fundamental Life cycle Approach', *Procedia CIRP*, The 24th CIRP Conference on Life Cycle Engineering, vol. 61, pp. 588–593, Jan. 2017, ISSN: 2212-8271. DOI: 10.1016/j.procir.2016.11.138.

[42] D. Stefanescu and R. Ruxanda, 'Fundamentals of solidification', in Feb. 2004, vol. 9, pp. 71–92, ISBN: 978-1-62708-177-1. DOI: 10.31399/asm.hb.v09.a0003724.

[43] M. ZAMANI, *Al-Si Cast Alloys - Microstructure and Mechanical Properties at Ambient and Elevated Temperature*, English, Department of Materials and Manufacturing SCHOOL OF ENGINEERING, JÖNKÖPING UNIVERSITY Jönköping Sweden 2015.

[44] J. C. Lippold, *Welding Metallurgy and Weldeability*. John Wiley and Sons, 2015.

[45] J. Hjelen, *Scanning elektron-mikroskopi*. SINTEF, avdeling for metallurgi. Metallurgisk institutt, NTH, 1986.

[46] M. Walock, 'Nanocomposite coatings based on quaternary metal-nitrogen and nanocarbon systems', Ph.D. dissertation, Nov. 2012.

[47] F. Leijon, S. Wachter, Z. Fu, C. Körner, S. Skjervold and J. Moverare, *A novel rapid alloy development method towards powder bed additive manufacturing, demonstrated for binary Al-Ti, -Zr and -Nb alloys*, English, Materials and Design, 2021, https://doi.org/10.1016/j.matdes.2021.110129.

[48] N.-K. Tang, J. Chen and H.-Y. Hung, 'Effect of silicon on thermal conductivity of Al-Si alloys', *Materials Science and Technology Conference and Exhibition 2013, MS and T 2013*, vol. 2, pp. 1339–1343, 2013.

[49] R. Cao, J. X. Jiang, C. Wu and X. S. Jiang, 'Effect of addition of Si on thermal and electrical properties of Al-Si-Al $_2$ O $_3$ composites', English, *IOP Conference Series: Materials Science and Engineering*, vol. 213, p. 012 001, Jun. 2017, ISSN: 1757-8981, 1757-899X. DOI: 10.1088/1757-899X/213/1/012001.

[50] T. Ullsperger, G. Matthäus, L. Kaden, M. Rettenmayr, S. Risse and S. Nolte, 'Selective laser melting of AlSi40 using ultrashort laser pulses for additive manufacturing applications', p. 7,

[51] D. Furrer and S. Semiatin, 'Electrical Conductivity of Metals and Alloys', Dec. 2009. DOI: 10.31399/asm.hb.v22a.a0005445.

[52] *Sigmatest 2.069 – Operating Instructions*. FOERSTER.

[53] P. Zhang, S. Li and Z. Zhang, *General relationship between strength and hardness*, English, Materials Science and Engineering: A, Volume 529, 2011, Pages 62-73, ISSN 0921-5093. https://doi.org/10.1016/j.msea.2011.08.061.

[54] D. Herzog, V. Seyda, E. Wycisk and C. Emmelmann, *Additive manufacturing of metals*, English, Acta Materialia, Volume 117, 2016, Pages 371-392. https://doi.org/10.1016/j.actamat.2016.07.019.

[55] K. Kashyap and T. Chandrashekar, *Effects and mechanisms of grain refinement in aluminium alloys*, English, Bull Mater Sci 24, 345–353 (2001). https://doi.org/10.1007/BF02708630.

[56] F. Wang, D. Qiu, Z.-L. Liu, J. A. Taylor, M. A. Easton and M.-X. Zhang, *The grain refinement mechanism of cast aluminium by zirconium*, English, Acta Materialia, Volume 61, Issue 15, 2013, Pages 5636-5645, ISSN 1359-6454. https://doi.org/10.1016/j.actamat.2013.05.044.

[57] D. Carluccio, M. Bermingham, Y. Zhang *et al.*, *Grain refinement of laser remelted Al-7Si and 6061 aluminium alloys with Tibor® and scandium additions*, English, Journal of Manufacturing Processes, Volume 35, 2018, Pages 715-720. https://doi.org/10.1016/j.jmapro.2018.08.030.

[58] A. Djuraev, *Porosity Reduction and Characterization of Aluminium Components Produced by Additive Manufacturing*, Master thesis, 2017.

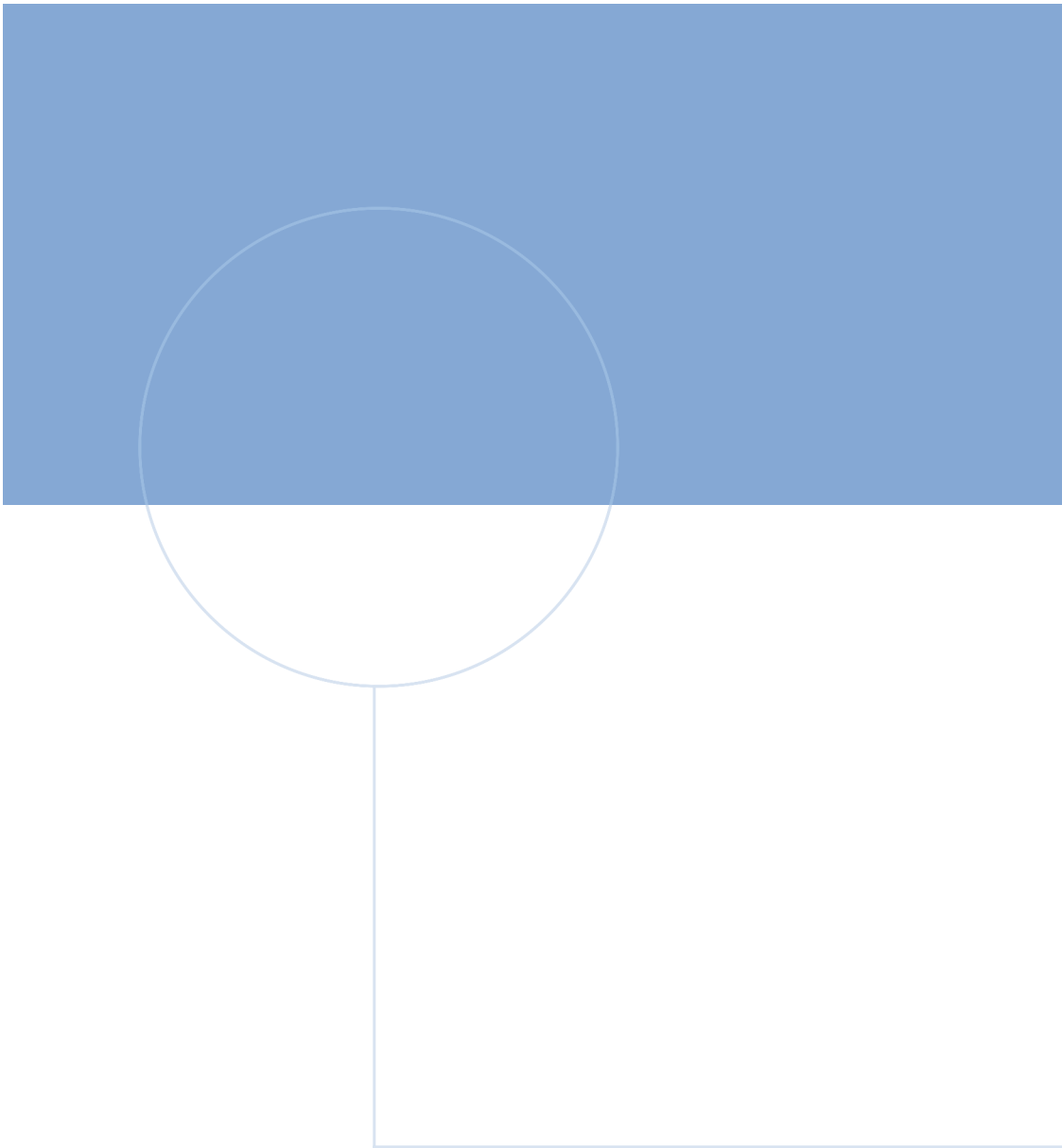

NTNU

Norwegian University of
Science and Technology